Elasto-plastic truss optimization under geometric nonlinearity using a genetic algorithm

Péter Grubits
Department of Structural and Geotechnical Engineering, Széchenyi István University, Győr, Hungary
grubits.peter@sze.hu, https://orcid.org/0009-0002-0451-0959

Pálma Porrogi
Department of Theorethical Health Sciences, Széchenyi István University, Győr, Hungary
Centre of Translational Medicine, Semmelweis University, Hungary
porrogi.palma@sze.hu, https://orcid.org/0009-0004-6554-0304

Majid Movahedi Rad
Department of Structural and Geotechnical Engineering, Széchenyi István University, Győr, Hungary
majidmr@sze.hu, https://orcid.org/0000-0002-8393-724X

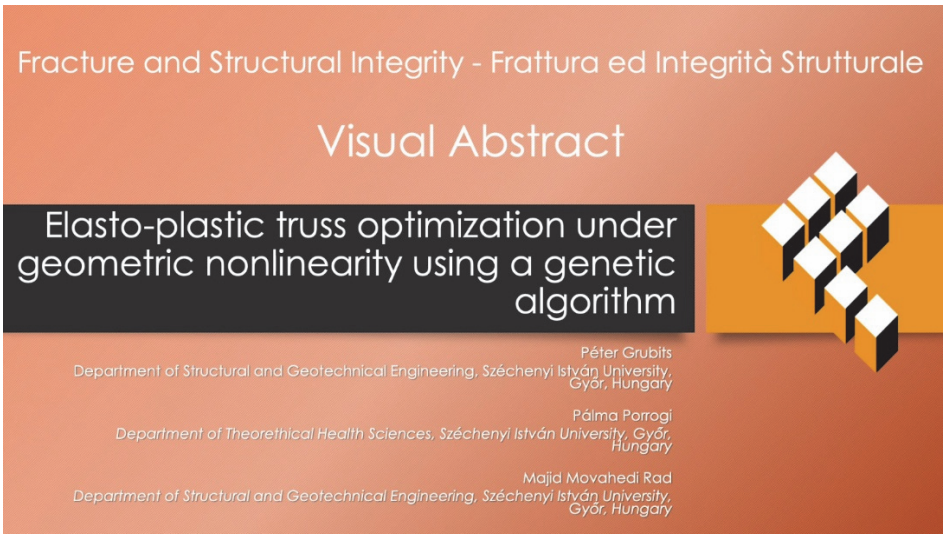

Citation: Grubits, P., Porrogi, P., Movahedi Rad, M., Elasto-plastic truss optimization under geometric nonlinearity Using a genetic algorithm, Fracture and Structural Integrity, 75 (2026) 124-156.

Received: 09.09.2025
Accepted: 06.10.2025
Published: 21.10.2025
Issue: 01.2026

KEYWORDS. Structural optimization, steel trusses, elasto-plastic analysis, geometric nonlinearity, finite element method, genetic algorithm.

INTRODUCTION

Steel trusses are widely used in various structural applications owing to their numerous advantages, particularly their excellent strength-to-weight ratio and structural flexibility. The most common applications include bridges, roofs, and transmission towers, where proper design is essential to ensure safety and reliability. However, under unexpectedly excessive loads—such as extreme weather conditions [1] or seismic events [2]—trusses may experience significant stress

and deformation near collapse, which can exceed the assumptions of conventional computational methods. Specifically, in such extraordinary situations, nonlinear effects—including yielding and large displacements—become significant and must be accounted for to achieve accurate predictions of structural behavior. This demonstrates the necessity for advanced design strategies capable of capturing complex nonlinear responses and providing safer and more efficient solutions beyond the limitations of traditional approaches.

In this context, plastic analysis offers a promising approach for enhancing structural design and mitigating the risk of catastrophic collapse. Depending on the structural type and boundary conditions, failure may be governed by the yielding of the members. Accordingly, plastic analysis focuses on the identification and assessment of inelastic deformations that accumulate and persist after unloading. Among the various theorems developed in recent decades [3–5], a notable solution method for elasto-plastic analysis is the work of Kaliszky [6], who introduced a nonlinear mathematical program for control of plastic performance. Building upon this work, Kaliszky and Lógó [7] proposed a design method for optimizing bar structures, which incorporates the complementary strain energy of residual forces to characterize plastic deformations. This approach was later extended to address the strengthening of elasto-plastic trusses [8]. In these studies, the developed technique was demonstrated using a geometrically perfect 9-bar structure, under the assumption of small displacements and solved using a gradient-based optimization algorithm.

Beyond the consideration of plastic behavior, the effect of large deformations is critical for accurately capturing the structural response [9], particularly in relatively slender trusses [10], where such deformations contribute significantly to geometric nonlinearity. Over the years, the finite element method (FEM) has proven to be a robust and versatile tool in this context [11–13], employing incremental–iterative solution strategies that systematically update the stiffness matrix to reflect the evolving stress–strain relationship during deformation. Based on this groundwork, several researchers have developed optimization frameworks for truss structures that explicitly incorporate geometric nonlinearity [14–16].

To ultimately improve the design of truss structures, increasing emphasis has recently been placed on integrating inelastic behavior and geometric nonlinearity within a unified optimization framework. Viet-Hung and Seung-Eock [17] proposed a reliability-based optimization approach aimed at minimizing structural weight, incorporating constraints related to strength, displacement, and failure probability. Subsequently, Viet-Hung et al. [18] introduced a machine learning-based method for size optimization that considers both serviceability and load-bearing requirements. Expanding on this, Viet-Hung et al. [19] further enhanced the optimization algorithm by integrating additional machine learning techniques. It is noteworthy that all three studies assumed initially perfect structural geometry and did not incorporate plastic analysis for the control of inelastic deformations. In contrast, Grubits and Movahedi [20] developed a novel optimization framework for elasto-plastic trusses, which integrates plastic behavior within a geometrically nonlinear context and allows for the inclusion of initial geometric imperfections. While earlier approaches—such as those proposed by Kaliszky and Lógó [6–8]—successfully addressed plastic behavior through complementary strain energy under the assumption of small displacements, the recent framework extends this capability to structures subjected to large deformations and imperfection-sensitive responses.

Building upon the earlier work of the Authors presented in [20], this research further advances the previously developed framework by incorporating serviceability constraints to limit displacements in accordance with code-based criteria, thereby enhancing the robustness and practical applicability of the proposed optimization approach. Consequently, an advanced design methodology is introduced for the elasto-plastic and elastic analysis of steel trusses. This is achieved by assessing and limiting plastic deformations through the complementary strain energy of residual forces, and by employing an incremental solution technique based on the finite element method to account for geometric nonlinearity. The proposed mathematical formulations enable a careful and rigorous design process in which, alongside the objective of minimizing structural weight, three penalty terms—related to load-bearing capacity, inelastic behavior, and global stability—ensure that the final solution is both materially efficient and structurally safe.

Ultimately, this approach allows for a precise characterization of structural response, with the capability to capture various failure modes such as elastic buckling, yielding, and inelastic post-buckling. By incorporating a newly introduced displacement constraint, serviceability requirements can also be directly addressed in the design process. This comprehensive and flexible framework offers a versatile design tool that accommodates a wide range of performance criteria and practical constraints. In this way, the methodology not only overcomes the limitations of conventional elastic design practices but also offers a practical computational framework that balances efficiency with reliability. By explicitly linking advanced nonlinear analysis with optimization, the study demonstrates how modern mathematical tools such as genetic algorithms can be effectively leveraged to deliver innovative solutions for the safe and sustainable design of steel trusses.

The effectiveness and capability of the proposed methodology are demonstrated through two widely recognized benchmark examples—the 37-bar planar truss and the 25-bar space truss. For the 37-bar truss, two primary design scenarios are investigated: (i) elastic design, where structural adequacy is ensured without any inelastic deformation while satisfying the required load-bearing capacity, and (ii) elasto-plastic design, in which plastic deformations are permitted but constrained

within an acceptable limit under the applied load. In addition, a supplementary optimization case is conducted in the elasto-plastic scenario by imposing displacement thresholds to assess the influence of serviceability requirements. In the 25-bar truss example, the analysis focuses exclusively on elasto-plastic design, where two cases are compared: one without displacement constraints and another where serviceability limitations are explicitly enforced. The obtained results confirm the efficiency of the developed framework, underlining the practical relevance of advanced optimization techniques in improving structural design precision and achieving safer, more materially efficient configurations.

THEORETICAL FOUNDATION FOR MATERIAL AND GEOMETRICAL NONLINEAR ANALYSIS

This section outlines the fundamental theoretical components underlying the proposed framework. First, the complementary plastic work theory is introduced, which serves as the methodological basis by providing a physically meaningful measure of plastic deformations. Building on this foundation, the principles of elastic and elasto-plastic limit analysis are discussed, with particular emphasis on the role of complementary strain energy associated with residual forces. Finally, the core aspects of geometrically nonlinear analysis are presented, as incorporated into the structural design process to accurately reflect the behavior of structures under large deformations.

Complementary plastic work theory

This section outlines the theoretical basis of the complementary plastic work theory. Consider a model composed of an elasto-plastic material, assumed to be independent of both time and temperature. The body occupies a volume V and is bounded by a surface S, which is partitioned into two disjoint subsets: S_u, where zero surface displacement is prescribed, and S_q, which is subjected to quasi-static surface tractions $q(t,x_i)$, with x_i denoting the position vector on the surface. Following the foundational work of Kaliszky [6], the field quantities at a given time t are defined as follows:

$\sigma_{ij}(t)=$ actual stress components,

$\in_{ij}(t)$ and $u_i(t)$ = actual strain and displacement fields,

$\sigma_{ij}^{el}(t)=$ fictitious stress components corresponding to an ideal purely elastic response,

$\varepsilon_{ij}^{el}(t)$ and $u_i^{el}(t)=$ fictitious elastic strains and displacements associated with $\sigma_{ij}^{el}(t)$.

To further characterize the internal force state, two additional stress fields are introduced:

$\sigma_{ij}^{R}(t)=$ the actual residual stress distribution,

$\bar{\sigma}_{ij}^{R}=$ any arbitrary, time-independent self-stress distribution.

According to the constitutive relation for time-independent elasto-plastic materials, the total strain ε_{ij} can be additively decomposed into elastic and plastic components:

$$\varepsilon_{ij}=\varepsilon_{ij}^{el}+\varepsilon_{ij}^{pl} \tag{1}$$

This relation is assumed to hold at every time step throughout the loading history. Consequently, the material behavior does not involve any intrinsic time dependence, and the evolution of inelastic strains can be fully described within a rate-independent framework.

The elastic strain is related to the actual stress tensor via the fourth-order elastic stiffness tensor C_{ijkl}, assuming linear elasticity:

$$\varepsilon_{ij}^{el}=C_{ijkl}\sigma_{kl} \tag{2}$$

Meanwhile, the evolution of plastic strain is governed by the associated flow rule [6]:

$$\dot{\varepsilon}_{ij}^{pl}=\dot{\lambda}\frac{\partial f}{\partial \sigma_{ij}},\ \dot{\lambda}\geq 0\ \textit{if}\ f=0\ \textit{and}\ \dot{f}=0,\ \textit{otherwise}\ \dot{\lambda}=0 \tag{3}$$

where f denotes the yield function and $\dot{\lambda}$ is the plastic multiplier, as schematically illustrated for the von Mises yield surface under plane stress in Fig. 1.

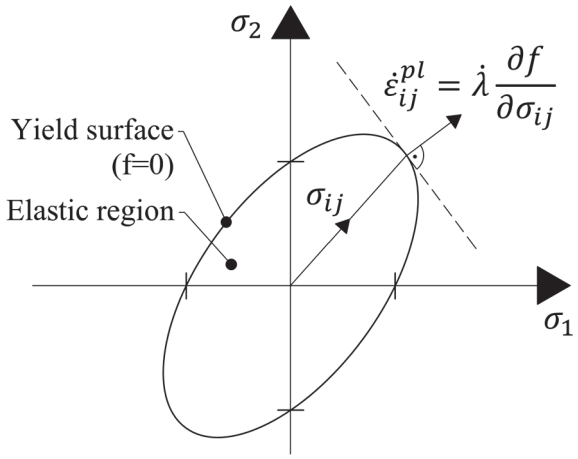

Figure 1: Schematic illustration of the associated flow rule for the von Mises yield surface under plane stress conditions.

Considering again the body introduced earlier, the total stress field $\sigma_{ij}(t)$ at time t can be expressed, in accordance with the constitutive relations presented in Eqns. (1) and (2), as the sum of a fictitious elastic stress component $\sigma_{ij}^{el}(t)$, corresponding to the elastic part of the total strain, and a time-independent residual stress component σ_{ij}^{R}, which accounts for the irreversible effects of plastic deformation:

$$\sigma_{ij}(t) = \sigma_{ij}^{el}(t) + \sigma_{ij}^{R} \tag{4}$$

The fictitious elastic strain field $\varepsilon_{ij}^{el}(t)$, associated with the fictitious elastic stress $\sigma_{ij}^{el}(t)$, is related to the stress field through the linear elastic constitutive relation introduced in Eqn. (2):

$$\varepsilon_{ij}^{el}(t) = C_{ijkl}\sigma_{kl}^{el}(t) \tag{5}$$

It should be emphasized that Eqns. (2) and (5) refer to different stress fields: Eqn. (2) involves the actual stress $\sigma_{ij}(t)$, while Eqn. (5) is defined in terms of the fictitious elastic stress $\sigma_{ij}^{el}(t)$. These are connected through the decomposition in Eqn. (4), where the residual stress σ_{ij}^{R} does not vanish.

This stress decomposition facilitates the evaluation of the complementary strain energy associated with the residual stress field, offering a scalar quantity to characterize inelastic behavior within the elasto-plastic framework. To further clarify this concept, consider the total complementary plastic work accumulated along a loading path from $t = 0$ to $t = \tau$. This work serves as a meaningful measure for quantifying the extent of plastic deformation and evaluating the inelastic performance of the body under consideration.

If a time-independent, self-equilibrated stress field $\bar{\sigma}_{ij}^{R}$ can be identified such that the following yield condition is satisfied throughout the volume V at any time $t \le \tau$:

$$f\left(\sigma_{ij}^{el}(t) + \bar{\sigma}_{ij}^{R}\right) \le 0 \tag{6}$$

then the total complementary plastic work $W_p(\tau)$ is bounded from above by the expression:

$$W_p(\tau) \le \frac{1}{2}\int C_{ijkl}\bar{\sigma}_{ij}^{R}\bar{\sigma}_{kl}^{R}dV \tag{7}$$

To control the extent of plastic deformation, an upper limit W_{p0} is prescribed on the allowable complementary plastic work W_p. This constraint is enforced by relating the limit directly to the actual residual stress distribution. Specifically, it is assumed that:

$$\bar{\sigma}_{ij}^{R} \equiv \sigma_{ij}^{R} \tag{8}$$

This identification yields a conservative and practical estimate, enabling the formulation of a tractable constraint on allowable plastic work. The resulting condition that limits plastic dissipation takes the form:

$$W_p = \frac{1}{2}\int C_{ijkl}\sigma_{ij}^{R}\sigma_{kl}^{R}dV - W_{p0} \le 0 \tag{9}$$

Elastic and elasto-plastic limit analysis based on residual forces

To establish a load-dependent response, assume that the surface traction $\boldsymbol{q}(t,x_i)$ applied to the body occupying volume V, is defined as:

$$q(t,x_i) = m(t)q_0(x_i), 0 \le t \le \tau \tag{10}$$

where $m(t)$ is a time-dependent load multiplier that increases monotonically, and $q_0(x_i)$ is a time-independent surface load distribution defined over the surface S_q.

In the case of truss structures with constant structural weight $G_s = \rho\sum_{i=1}^{n} A_i l_i$ where ρ is the material density, A_i is the cross-sectional area, and l_i is the length of the i-th bar, the loading expression can be reformulated in terms of the externally applied nodal load vector $\boldsymbol{P}_0$ and a prescribed reference load $\boldsymbol{P}$, such that:

$$\boldsymbol{P}_0 = m\boldsymbol{P} \tag{11}$$

Throughout the loading history, the maximum value of the load multiplier m for which all bar elements remain within the elastic range is denoted by m_{el}. Consequently, the corresponding elastic limit load $\boldsymbol{P}^{el}$ is given by:

$$\boldsymbol{P}^{el} = m_{el}\,\boldsymbol{P} \tag{12}$$

Up to this point, no plastic deformations occur in any of the individual members, and the structural response remains entirely elastic. Accordingly, the elastic internal force vector corresponding to the applied external load $\boldsymbol{P}_0$ can be expressed as:

$$\boldsymbol{N}^{el} = \boldsymbol{F}^{-1}\boldsymbol{G}^{T}\boldsymbol{K}^{-1}\boldsymbol{P}_0 \tag{13}$$

where $\boldsymbol{F}$ denotes the flexibility matrix, $\boldsymbol{G}$ is the geometric matrix, and $\boldsymbol{K}$ is the global stiffness matrix.

However, once the load exceeds $\boldsymbol{P}^{el}$, plastic deformations begin to develop in certain members and continue to evolve until the plastic collapse multiplier m_{pl} and its corresponding load level $\boldsymbol{P}^{pl}$ are reached:

$$\boldsymbol{P}^{pl} = m_{pl}\,\boldsymbol{P} \tag{14}$$

At this point, excessive plastic deformations prevent the internal stresses from equilibrating the externally applied load $\boldsymbol{P}_0$. Consequently, for load multipliers in the range $m_{el} \le m \le m_{pl}$ a residual internal force vector $\boldsymbol{N}^{R}$, representing the remaining forces after unloading, can be defined as the difference between the plastic internal force $\boldsymbol{N}^{pl}$ and the elastic component $\boldsymbol{N}^{el}$:

$$\boldsymbol{N}^{R} = \boldsymbol{N}^{pl} - \boldsymbol{N}^{el} \tag{15}$$

In this context, for a truss structure of structural weight G_s, the complementary strain energy associated with the residual forces can be expressed as:

$$W_p = \frac{1}{2E}\sum_{i=1}^{n}\frac{l_i}{A_i}\left(N_i^{R}\right)^2 \le W_{p0} \tag{16}$$

where E is the elasticity modulus of the material, N_i^{R} denote the residual force of the i-th bar, and W_{p0} represents the allowable limit of plastic deformation in the structure, beyond which the internal stresses can no longer maintain equilibrium, leading to structural collapse.

During elastic limit analysis, the primary objective is to determine the elastic load multiplier m_{el} for a structure with a given volume V and corresponding structural weight G_s, and to compute the associated elastic limit load $\boldsymbol{P}^{el}$, provided that the condition $W_p = 0$ remains satisfied. In contrast, the aim of elasto-plastic limit analysis is to determine the maximum load multiplier m such that the complementary plastic work satisfies the inequality $W_p \le W_{p0}$. To improve safety and enable precise control over inelastic deformations, a more restrictive threshold $0 < W_{p,max} \le W_{p0}$ may be specified, corresponding to the elasto-plastic limit load P^{ep} and its associated multiplier m_{ep}:

$$\boldsymbol{P}^{ep} = m_{ep}\,\boldsymbol{P} \tag{17}$$

The response curves in Fig. 2 schematically illustrate the identification of the three characteristic loads over the loading history of a representative truss (Fig. 2(a)). In Fig. 2(b), the load–plastic deformation diagram starts at $W_p = 0$; the elastic limit P^{el} is read at the last equilibrium state that still satisfies $W_p = 0$. The elasto-plastic limit P^{ep} is obtained at the prescribed threshold $W_{p,max}$ (with $0 < W_{p,max} \le W_{p0}$), such that $W_p = W_{p,max}$ and $P^{ep} = m_{ep}P$. Finally, the plastic limit P^{pl} corresponds to the maximum sustained load on the path. For clarity, the ordinate is marked at $\{P^{el}, P^{ep}, P^{pl}\}$, highlighting the progression from the purely elastic regime to controlled inelasticity and, ultimately, to the plastic limit. Fig. 2(c) reports the associated displacement history, which is consistent with the transitions observed on the load–plastic deformation curve and confirms that P^{ep} is reached well before plastic collapse.

This implies that, according to structural design criteria, a limited and controlled level of inelastic deformation may be permitted for a structure of given weight G_s. Alternatively, the elastic and elasto-plastic limit analysis problem can be reformulated as an optimization task, where the primary objective is to attain a prescribed load multiplier—corresponding to the target load $\boldsymbol{P}_0$—while minimizing the structural weight G_s. Within this framework, the cross-sectional areas A_i of the individual members serve as design variables, framing the task as a size optimization problem, which is one of the three principal categories of structural optimization [21].

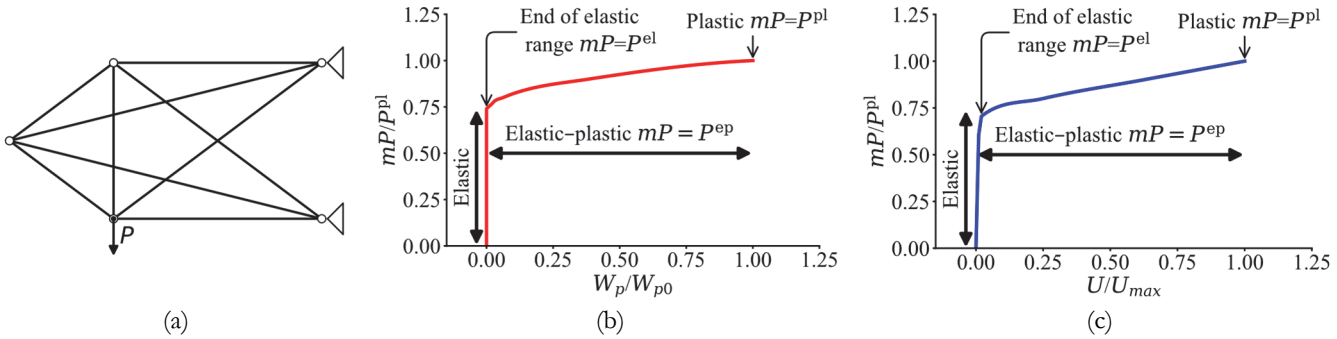

Figure 2: Identification of elastic, elasto-plastic, and plastic limits for a representative truss: (a) loading and support scheme; (b) load–plastic deformation response; (c) load–displacement response.

Geometrical nonlinear finite element analysis

Building upon the previously established linear-elastic and elasto-plastic framework, this section extends the analysis to account for geometric nonlinearities that arise in structures undergoing large deformations. In certain structural systems, such as slender truss configurations, large displacements and rotations may significantly affect the mechanical response. To accurately capture such behavior, the analysis must incorporate geometric nonlinearity within a total Lagrangian finite element framework. In this formulation, the Green–Lagrange strain tensor ε_{ij} and the second Piola–Kirchhoff stress tensor s_{ij} are employed. These quantities form a work-conjugate pair suitable for the analysis of large deformations while remaining consistent with the underlying constitutive laws.

The Green–Lagrange strain tensor is defined as:

$$\varepsilon_{ij} = \frac{1}{2}\left(u_{i,j} + u_{j,i} + u_{k,i}u_{k,j}\right) \tag{18}$$

where u denotes the displacement field, and indices i, j, k refer to spatial directions.

In finite element implementations, the incremental form of the strain–displacement relationship is written as:

$$d\boldsymbol{\varepsilon} = \boldsymbol{B}(\boldsymbol{U})\,d\boldsymbol{U} \tag{19}$$

where $\boldsymbol{B}(\boldsymbol{U})$ is the displacement-dependent strain–displacement matrix and $d\boldsymbol{U}$ is the vector of incremental nodal displacements. The matrix $\boldsymbol{B}(\boldsymbol{U})$ evolves with the current configuration, capturing the geometric nonlinearity of the deformation process.

In consistency with the previously presented Eqn. (2), the constitutive relation in terms of the Green–Lagrange strain tensor and the second Piola–Kirchhoff stress tensor is expressed as:

$$s_{ij} = C_{ijkl}\varepsilon_{kl} \tag{20}$$

To assess equilibrium in the deformed configuration, the global residual vector is defined as:

$$\boldsymbol{R}(\boldsymbol{U}) = \boldsymbol{P}_0 - \int \boldsymbol{B}^T \boldsymbol{s}\,dV \tag{21}$$

where $\boldsymbol{P}_0$ is the vector of externally applied loads, and $\boldsymbol{s}$ represents the current second Piola–Kirchhoff stress field. The residual vector $\boldsymbol{R}(\boldsymbol{U})$ quantifies the imbalance between internal and external forces and vanishes when equilibrium is satisfied.

The nonlinear equilibrium equations are solved iteratively using the Newton–Raphson method, in which the tangent stiffness matrix is computed as:

$$\boldsymbol{K}_T = \frac{\partial \boldsymbol{R}}{\partial \boldsymbol{U}} \tag{22}$$

This iterative scheme updates the displacement field until convergence is achieved, enabling the simulation of both elastic and elasto-plastic behavior under geometric nonlinearity. The resulting displacement vector $\boldsymbol{U}$, representing the total nodal displacements at equilibrium, becomes a key quantity in the assessment of deformation-based criteria, such as serviceability. As such, it may also serve as the basis for imposing constraints on maximum allowable displacements in subsequent optimization formulations.

Importantly, this geometrically nonlinear formulation remains fully consistent with the residual force–based framework and the evaluation of complementary plastic work introduced earlier. The use of Green–Lagrange strains and second Piola–Kirchhoff stresses ensures a coherent treatment of both material and geometrical nonlinearities, enabling accurate assessment of residual internal forces and the corresponding inelastic energy contributions throughout the deformation history. Furthermore, by operating within a total Lagrangian framework, this approach inherently allows the incorporation of initial geometric imperfections, which can significantly influence the structural response—particularly in slender systems sensitive to stability effects.

OPTIMIZATION

Expanding on the foundational concepts discussed in the preceding sections, this part of the study presents the mathematical formulation of two optimization problems: one based on elastic limit analysis and the other on elasto-plastic limit analysis. The proposed formulations are integrated into a unified computational framework, enabling flexible and accurate structural design under both material and geometrical nonlinearities.

Elastic design optimization

In the context of elastic limit analysis, the principal objective is to determine the elastic limit load $\boldsymbol{P}^{el}$, which marks the onset of yielding in a structural system characterized by a given configuration and associated structural weight G_s. Beyond this threshold, plastic deformations begin to develop. Based on this theoretical foundation, the elastic design problem is formulated as an optimization task, where the aim is to minimize the structural weight G_s while ensuring that the structural response remains entirely elastic and that sufficient global stability is maintained. This approach enables a design strategy that is simultaneously material-efficient and structurally robust, expressed mathematically as follows:

$$min: fitness = f\left(G_s\right) + p_1\left(m\boldsymbol{P}\right) + p_2\left(\bar{\lambda}\right) \tag{23a}$$

where the objective function "*fitness*" quantifies the overall quality of a given design solution based on three components: the structural weight term $f\left(G_s\right)$, and two penalty terms, $p_1\left(m\boldsymbol{P}\right)$ and $p_2\left(\bar{\lambda}\right)$, which enforce the elastic limit and stability conditions, respectively. The function $f\left(G_s\right)$ aims to minimize the total structural weight within prescribed design bounds, using a normalized expression that incorporates the minimum and maximum allowable cross-sectional areas A_{min} and A_{max}, which together define the design domain. Accordingly, $f\left(G_s\right)$ is expressed as:

$$f\left(G_s\right) = \rho\left(\frac{\sum_{i=1}^{n} A_i l_i + \sum_{i=1}^{n} A_{min} l_i}{\sum_{i=1}^{n} A_{max} l_i + \sum_{i=1}^{n} A_{min} l_i}\right) \tag{23b}$$

For further clarification, the term $p_1\left(m\boldsymbol{P}\right)$ is introduced to ensure that the optimized structure reaches the predefined load level $\boldsymbol{P}_0$, while remaining within the elastic regime and avoiding failure due to instability or yielding. This term evaluates the extent to which the structure satisfies the fundamental design requirement of attaining the desired load-carrying capacity. The formulation distinguishes between four physically meaningful scenarios that may arise during the load history:

$$p_1(m\boldsymbol{P}) = \begin{cases} 0, if\ \boldsymbol{P}^{el} \geq \boldsymbol{P}_0\ and\ mP \geq \boldsymbol{P}_0 \\ 1 - \dfrac{\boldsymbol{P}^{el}}{\boldsymbol{P}_0}, if\ \boldsymbol{P}^{el} < \boldsymbol{P}_0\ and\ mP \geq \boldsymbol{P}_0 \\ 1 - \dfrac{m\boldsymbol{P}}{\boldsymbol{P}_0}, if\ mP < \boldsymbol{P}_0\ and\ \boldsymbol{P}^{el} \geq m\boldsymbol{P} \\ 1 - \dfrac{\boldsymbol{P}^{el}}{\boldsymbol{P}_0}, if\ mP < \boldsymbol{P}_0\ and\ \boldsymbol{P}^{el} < m\boldsymbol{P} \end{cases} \tag{23c}$$

Here, $m\boldsymbol{P}$ denotes the maximum load attained during the load history, as determined by the load multiplier m, while $\boldsymbol{P}^{el}$ represents the elastic limit load marking the onset of yielding, in accordance with the principles of elastic limit analysis. The interpretation of each case is as follows:

- Case 1: The structure remains entirely elastic and reaches or exceeds the target load $\boldsymbol{P}_0$; no penalty is applied.
- Case 2: Plastic yielding occurs before reaching $\boldsymbol{P}_0$; a penalty is applied based on the shortfall in $\boldsymbol{P}^{el}$.
- Case 3: The structure remains elastic but is unable to reach $\boldsymbol{P}_0$ due to elastic instability, such as buckling of individual bar members; the penalty is based on the attained load $m\boldsymbol{P}$.
- Case 4: The structure fails to reach $\boldsymbol{P}_0$ and plastic deformations occur before instability; in this case, the penalty is again based on $\boldsymbol{P}^{el}$.

This formulation ensures that the optimization process prioritizes solutions that are both material-efficient and structurally robust, guiding the design toward configurations capable of safely withstanding the target load without yielding or buckling. In addition to achieving the required load-bearing capacity, practical structural design often necessitates enforcing a minimum threshold for the critical buckling load factor, denoted by $\bar{\lambda}$. This parameter is typically identified as the smallest eigenvalue obtained from linear buckling analysis (LBA), with its corresponding eigenvector $\bar{\phi}$ representing the critical buckling mode shape. To enhance structural safety and effectively guide the optimization process, a stability-based penalty function $p_2(\bar{\lambda})$ is introduced. This term penalizes configurations with inadequate global stability and is defined as:

$$p_2(\bar{\lambda}) = \begin{cases} 0, \ if\ \bar{\lambda} \geq \lambda_{stab} \\ 1 - \dfrac{\bar{\lambda}}{\lambda_{stab}}, \ if\ \bar{\lambda} < \lambda_{stab} \end{cases} \tag{23d}$$

where λ_{stab} denotes a prescribed threshold value for the critical buckling load factor, which can be freely selected in accordance with specific design requirements. If chosen to be relatively low, the influence of the stability penalty term becomes negligible. This formulation ensures that the optimization penalizes configurations with insufficient resistance to global buckling, thereby promoting structurally stable solutions that meet the prescribed safety criteria.

As presented through Eqns. (23b)–(23d), the structural weight term $f(G_s)$, along with the penalty terms $p_1(m\boldsymbol{P})$ and $p_2(\bar{\lambda})$, are formulated using normalized expressions. As a result, their values always lie within the range $[0,1]$. This solution ensures consistent scaling within the overall objective function and enables the coherent evaluation of competing design objectives—such as minimizing material usage, maintaining elastic behavior, and ensuring structural stability—within a unified optimization framework. Consequently, the proposed formulation facilitates an efficient and robust search for optimal solutions that effectively balance weight reduction with safety requirements.

In addition to the objective function and associated penalty terms, further constraints are imposed to enhance the effectiveness of the design process. These are defined as follows:

Subject to:

$$\max_{k} |U_k| \leq U_{max} \tag{23e}$$

$$W_p = \frac{1}{2E}\sum_{i=1}^{n}\frac{l_i}{A_i}\left(N_i^R\right)^2 = 0 \tag{23f}$$

$$\boldsymbol{X} = \boldsymbol{X}_0 + \Delta\boldsymbol{x} \text{ where } \Delta\boldsymbol{x} = \sum_{j}^{M}\boldsymbol{\phi}_j\omega_j \tag{23g}$$

Here, Eqn. (23e) introduces a displacement constraint that plays a critical role in ensuring structural serviceability, particularly in scenarios where excessive deformations may compromise performance or user comfort. In this context, U_k denotes the displacement component corresponding to the k-th degree of freedom in the global displacement vector $\boldsymbol{U}$, while U_{max} represents the prescribed maximum allowable displacement, defined in accordance with applicable serviceability criteria or design standards. This formulation offers the flexibility to impose displacement limits at any node and in any direction, thereby accommodating a wide range of functional design requirements. During the optimization process, this constraint may be omitted in cases where serviceability is not a governing design criterion or where the primary focus is structural strength and stability.

Furthermore, Eqn. (23f) expresses the elastic condition by requiring that the complementary plastic strain energy W_p remains zero. Incorporating the calculation of W_p during structural analysis enables the identification of the elastic limit load $\boldsymbol{P}^{el}$. As the load $m\boldsymbol{P}$ increases, the structure initially responds elastically, and the point at which W_p first becomes nonzero marks the onset of plastic deformation. At this point, the corresponding load multiplier m_{el} is defined, such that $\boldsymbol{P}^{el} = m_{el}\boldsymbol{P}$. This provides a physically meaningful and computationally consistent criterion for detecting the elastic threshold within the proposed framework. Ultimately, this constraint serves as a formal guarantee of structural performance in applications where inelastic behavior is not permissible.

Finally, Eqn. (23g) introduces the representation of initial geometric imperfections within the design formulation. Here, the structural geometry $\boldsymbol{X}$ is expressed as the sum of the perfect configuration $\boldsymbol{X}_0$ and an imperfection vector $\Delta\boldsymbol{x}$, which captures perturbations in the nodal positions. The term $\Delta\boldsymbol{x}$ is constructed as a linear combination of eigenmodes $\boldsymbol{\phi}_j$ derived from LBA, each scaled by a corresponding weighting factor ω_j that governs its amplitude. When imperfections are not considered, the geometry reduces to the undeformed state, $\boldsymbol{X} = \boldsymbol{X}_0$. Otherwise, the designer is provided with flexibility to incorporate selected buckling modes and their influence magnitudes, enabling a more realistic and stability-conscious design process.

The developed framework integrates all components presented in Eqns. (23a)–(23g), offering a comprehensive formulation for the elastic design scenario. In addition to its core features, the framework is structured to optionally incorporate the displacement constraint Eqn. (23e), and the representation of initial geometric imperfections Eqn. (23g). This modularity enables flexible adaptation to a wide range of structural requirements, allowing the designer to tailor the optimization process based on the specific demands of different structural systems and performance criteria.

Elasto-plastic design optimization

Building upon the elastic optimization scenario and integrating the theoretical framework of elasto-plastic limit analysis, an extended optimization formulation is proposed. In this approach, plastic deformations are permitted during the loading process but are restricted by a predefined threshold value $W_{p,max}$, representing the maximum allowable complementary strain energy for an acceptable design. This parameter must satisfy the condition $0 < W_{p,max} \le W_{p0}$, where W_{p0} denotes the upper bound of plastic deformation beyond which internal stresses can no longer maintain equilibrium, ultimately resulting in structural collapse. The value of $W_{p,max}$ can be freely specified in accordance with design codes, performance objectives, or regulatory requirements. While the primary objective remains the minimization of structural weight G_s, the extended formulation explicitly regulates the allowable inelastic response, thereby enabling more material-efficient designs compared to the purely elastic scenario. Accordingly, the complete optimization problem is reformulated as follows:

$$min: fitness = f\left(G_s\right) + p_1\left(m\boldsymbol{P}\right) + p_2\left(\bar{\lambda}\right) + p_3\left(W_p\right) \tag{24a}$$

$$f\left(G_s\right)=\rho\left(\frac{\sum_{i=1}^{n}A_i l_i+\sum_{i=1}^{n}A_{min} l_i}{\sum_{i=1}^{n}A_{max} l_i+\sum_{i=1}^{n}A_{min} l_i}\right) \tag{24b}$$

$$p_1\left(m\boldsymbol{P}\right)=\begin{cases}0, if\ m\boldsymbol{P}\geq\boldsymbol{P}_0\\ 1-\dfrac{m\boldsymbol{P}}{\boldsymbol{P}_0}, if\ m\boldsymbol{P}<\boldsymbol{P}_0\end{cases} \tag{24c}$$

$$p_2\left(\bar{\lambda}\right)=\begin{cases}0, if\ \bar{\lambda}\geq\lambda_{stab}\\ 1-\dfrac{\bar{\lambda}}{\lambda_{stab}}, if\ \bar{\lambda}<\lambda_{stab}\end{cases} \tag{24d}$$

$$p_3\left(W_p\right)=\begin{cases}0, if\ W_p\leq W_{p,max}\\ \dfrac{W_p-W_{p,max}}{W_{p0}-W_{p,max}}, if\ W_p>W_{p,max}\end{cases} \tag{24e}$$

Subject to:

$$\max_k\left|U_k\right|\leq U_{max} \tag{24f}$$

$$W_p=\frac{1}{2E}\sum_{i=1}^{n}\frac{l_i}{A_i}\left(N_i^R\right)^2\leq W_{p0} \tag{24g}$$

$$\boldsymbol{X}=\boldsymbol{X}_0+\Delta\boldsymbol{x}\ \text{ where }\ \Delta\boldsymbol{x}=\sum_{j}^{M}\phi_j\omega_j \tag{24h}$$

As shown in Eqn. (24a), a new penalty term $p_3\left(W_p\right)$ is introduced to constrain the extent of plastic deformations. According to Eqn. (24e), this penalty becomes active when the complementary strain energy of residual forces W_p exceeds the predefined threshold $W_{p,max}$. In such cases, the penalty is calculated using a normalized expression that depends on the attained value of W_p under the applied load level $m\boldsymbol{P}$, the allowable $W_{p,max}$, and W_{p0}. This normalization ensures that $p_3\left(W_p\right)$ remains bounded within the interval $[0,1]$, thereby maintaining consistent scaling across all penalty components. The inclusion of this term allows for precise control over the admissible inelastic behavior while ensuring compatibility with the overall design objectives and structural safety criteria.

In addition to the plasticity-related term $p_3\left(W_p\right)$, the penalty function $p_1\left(m\boldsymbol{P}\right)$ continues to play an essential role in the elasto-plastic design formulation, as structural failure may still occur without the development of plastic deformations—most notably due to elastic instability, such as buckling. However, as shown in Eqn. (24c), the formulation of $p_1\left(m\boldsymbol{P}\right)$ differs from its counterpart in Eqn. (23c), which was originally defined for the purely elastic design case. In the present elasto-plastic context, $p_1\left(m\boldsymbol{P}\right)$ is activated only if the structure fails to reach the predefined load level $\boldsymbol{P}_0$ during the loading history. This modification reflects the relaxation of the strict elastic requirement, as load levels exceeding $\boldsymbol{P}^{el}$ are now permitted. Consequently, the objective shifts toward ensuring that the target load $\boldsymbol{P}_0$ is achieved, while the extent of inelastic deformation is explicitly controlled through the complementary strain energy W_p, evaluated from the residual internal forces.

Moreover, in relation to the new penalty term, the constraint on complementary plastic work is updated, as expressed in Eqn. (23g), to ensure that the calculated W_p does not exceed W_{p0} . This constraint safeguards against configurations with excessive plasticity that would compromise the structural integrity of the design.
The developed framework is further extended by incorporating Eqns. (24a)–(24h), thereby enhancing its adaptability and broadening its functional capabilities. This comprehensive formulation enables a robust and advanced design methodology applicable across a wide range of structural scenarios.

DEVELOPED FRAMEWORK

This section presents the key components of the developed framework used for the automated design of truss structures under both elastic and elasto-plastic design scenarios, with the corresponding equations and concepts. The implementation was achieved by integrating PYTHON programming with the ABAQUS [22] commercial finite element software. In particular, the coding environment enabled the direct calculation of the complementary strain energy of residual forces (W_p), which is not available as a built-in feature in ABAQUS or other commercial design software. This capability was essential for establishing residual force–based design control within the optimization loop. Moreover, the framework was designed with flexibility: although the current implementation employs a genetic algorithm (GA) in combination with ABAQUS, both the optimization algorithm and the FE solver can be substituted with alternatives, provided they support the required nonlinear analysis capabilities. In this way, the developed workflow extends beyond the limitations of standard commercial packages by offering a fully automated and adaptable platform for advanced truss design.
The automatic operation of the proposed design methodology is driven by genetic algorithm (GA), a widely used metaheuristic optimization technique recognized for its robustness across various engineering applications. Inspired by the principles of natural selection, the GA iteratively refines a population of candidate solutions by optimizing a fitness function over successive generations. This fitness value quantifies the performance of each individual and plays a central role in guiding the evolutionary process, which is governed by genetic operators such as selection, crossover, and mutation.
To integrate the key components into a unified framework, the design process illustrated in Fig. 3 is adopted, utilizing a GA–driven optimization approach. In this study, a binary-encoded GA is employed, wherein design variables are represented as bit-string chromosomes. The optimization begins with the definition of design requirements, followed by the creation of an initial population. Subsequently, the fitness of each candidate solution is evaluated through a two-stage procedure involving linear buckling analysis (LBA) and geometrically and materially nonlinear analysis (GMNA). The generation is then refined using genetic operators to produce an offspring population. This iterative process continues until the predefined stopping criterion is met, which, as shown in Fig. 3, corresponds to reaching the last predefined generation of the GA. In practice, the total number of generations is specified in advance, and the algorithm terminates once this maximum number of iterations has been completed.

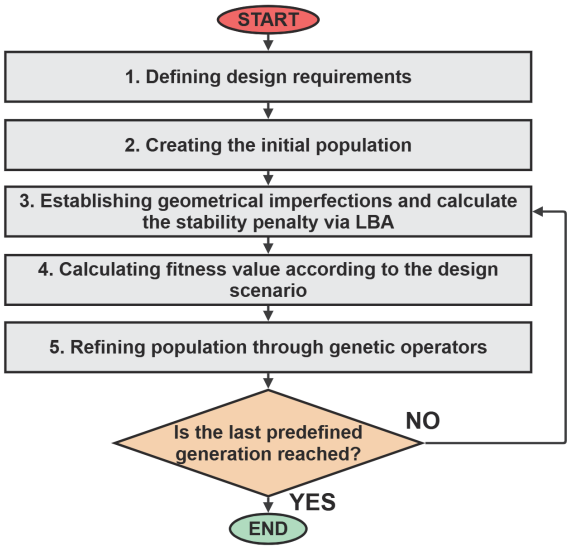

Figure 3: The main operation of the developed framework.

For further clarification, the procedure consists of the following steps:

1. Defining design parameters and requirements: The initial stage of the proposed framework, illustrated in Fig. 4, involves the definition of key parameters that delineate the design domain and associated criteria. First, the design scenario must be selected along with the specification of the applied external load $\boldsymbol{P}_0$. In case of elasto-plastic analysis, bounds for the complementary strain energy of the residual forces, $W_{p,max}$ and W_{p0}, should be established based on structural performance considerations.

   This stage also includes defining the permissible range of cross-sectional areas, namely the minimum A_{min}, maximum A_{max}, and the discrete step size A_s. Additional constraint parameters may be introduced as needed. To ensure global stability, a threshold value λ_{stab} for the critical buckling load factor can be prescribed. If serviceability requirements are considered, the maximum allowable displacement U_{max} may also be specified.

   Furthermore, the framework supports the incorporation of initial geometric imperfections derived from linear buckling analysis (LBA), offering full user control over the imperfection parameters. Two strategies are available: (i) automatic selection of the buckling mode shape ϕ_1 associated with the first positive eigenvalue $\lambda_1 = \overline{\lambda}$, which represents the critical buckling load factor, with the corresponding imperfection amplitude ω_1 determined as a function of the length L of the most sensitive structural member; or (ii) manual specification of one or more predefined mode shapes ϕ_j, with freely assigned amplitudes ω_j provided by the designer.

   As part of this stage, the parameters of the GA must also be defined. These include the number of generations (NG), population size (PS), crossover probability (CP), mutation probability (MP), tournament size (TS), and elitism size (ES). The specific values adopted in this study are summarized in Tab. 1.

Parameter	Value
Maximum number of generations (NG)	30
Population size (PS)	100
Crossover probability (CP)	0.7
Mutation probability (MP)	$0.1-0.9$
Tournament size (TS)	2
Elitism size (ES)	2

Table 1: Considered genetic algorithm parameters.

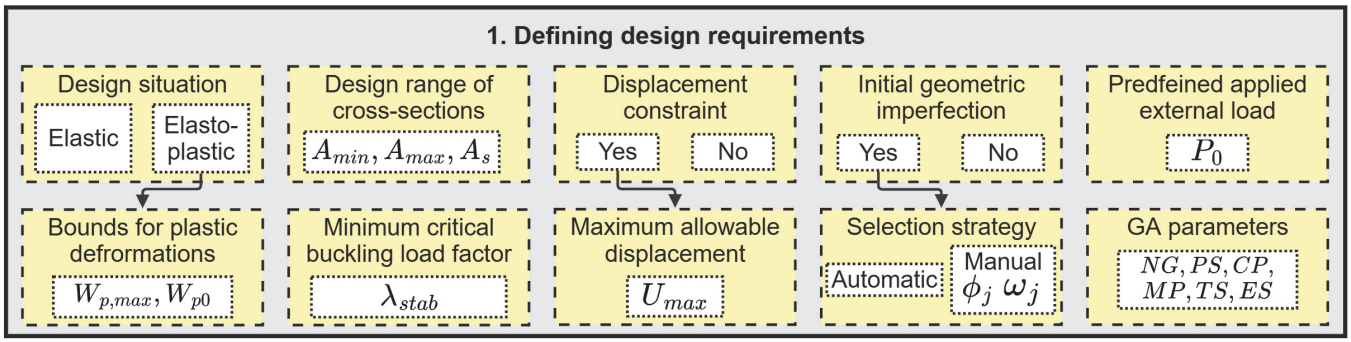

Figure 4: First stage of the developed framework.

2. Creating the initial population: In this step, a set of binary-encoded chromosomes is randomly generated according to the population size (PS). Each chromosome represents a candidate solution within the GA framework and is formulated with respect to the number of variables N_{var}, the predefined minimum area A_{min}, maximum area A_{max}, and discrete step size A_s. The binary chromosomes are then decoded into physical cross-sectional dimensions, which are subsequently used to automatically generate the corresponding finite element models. During this process, the structural weight G_s of each candidate design is also computed, as illustrated in Fig. 5.

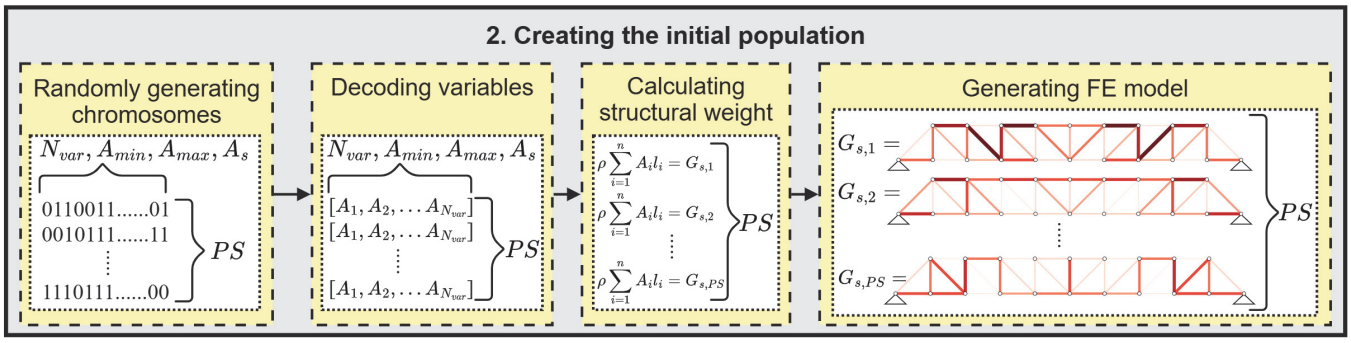

Figure 5: Second stage of the developed framework.

3. Establishing geometrical imperfections and determining the critical buckling load factor via LBA: A linear buckling analysis (LBA) is performed for each individual to extract the eigenvalues λ_j and the corresponding mode shapes ϕ_j, which are used to define the initial geometric imperfection $\Delta \boldsymbol{x}$. These imperfections are introduced in accordance with the design setup, ensuring consistency with the selected imperfection strategy, as illustrated in Fig. 6. In addition, the critical buckling load factor $\bar{\lambda}$ is identified and subsequently employed in the calculation of the stability-related penalty term $p_2(\bar{\lambda})$ which quantifies sensitivity to global instability and penalizes geometrically vulnerable configurations.

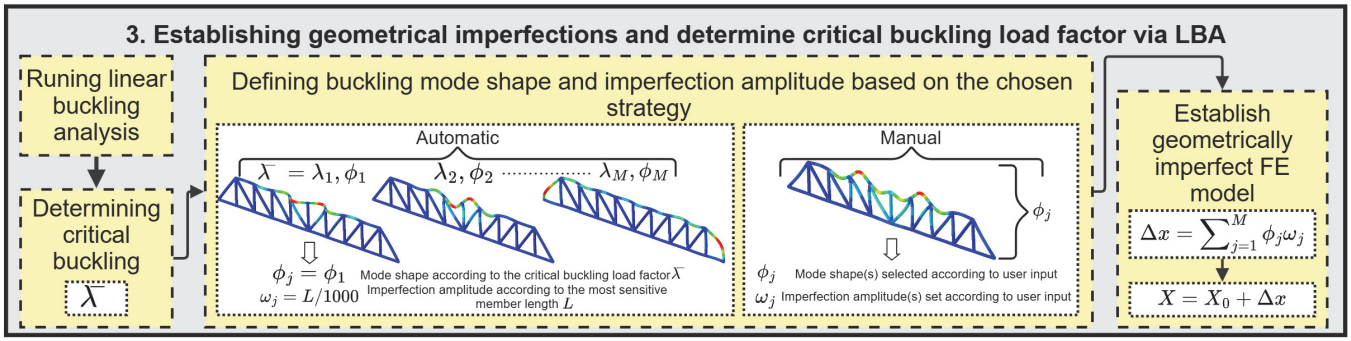

Figure 6: Third stage of the developed framework.

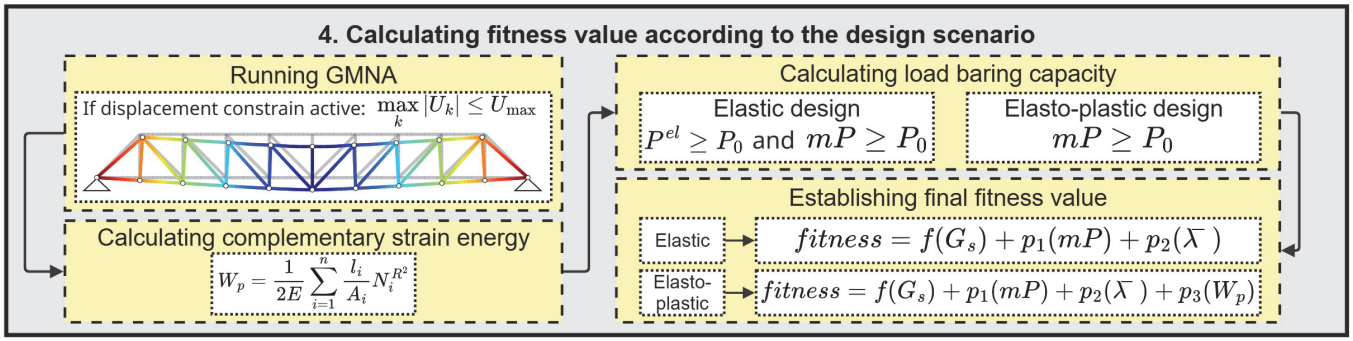

Figure 7: Fourth stage of the developed framework.

4. Calculating fitness value according to the design scenario: A geometrically and materially nonlinear analysis (GMNA) is carried out to simulate the full structural response under the applied loading history. When a displacement constraint is imposed, the analysis is terminated upon reaching the predefined limit U_{max} at the designated reference point, and the corresponding mechanical response values are extracted. Plastic deformations are quantified in the form of the accumulated complementary strain energy of residual forces, W_p. Depending on the design scenario, the penalty terms

$p_1(mP)$ and $p_3(W_p)$ are calculated. The final *fitness* value is established by combining the structural objective with the penalty contributions, thereby guiding the search toward feasible and physically meaningful solutions. The entire process is illustrated in Fig. 7.

5. Refining population through genetic operators: In the final stage, as illustrated in Fig. 8, the population is refined using genetic operators including tournament selection, uniform crossover, and mutation. These operators generate a new offspring population that gradually evolves toward improved design configurations. Parent candidates are identified via tournament selection, wherein randomly chosen subsets of the population are compared to select superior individuals. Genetic material is then recombined through uniform crossover, controlled by a specified crossover probability. To preserve genetic diversity, a dynamically adjusted mutation rate introduces random variations into the offspring. An elitism strategy ensures that the best-performing individual is retained across generations, maintaining solution quality throughout the optimization process. Steps 3 to 5 are repeated iteratively until the stopping criterion is satisfied, which, in this framework, corresponds to reaching the final generation.

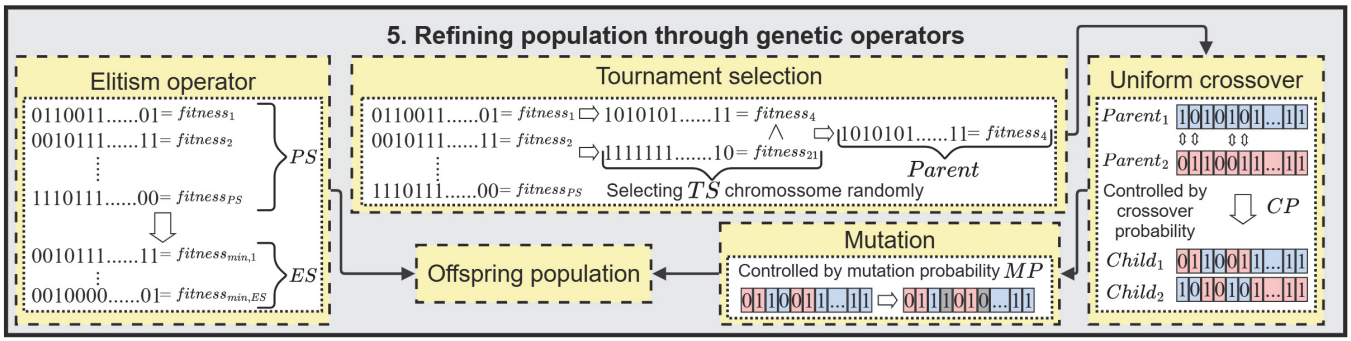

Figure 8: Fifth stage of the developed framework.

BENCHMARK NUMERICAL EXAMPLE: 37-BAR PLANAR TRUSS

This section presents a benchmark numerical example to evaluate the performance of the developed framework. To this end, three different optimization setups are applied to the same 37-bar truss structure. As a result, a comparative assessment of the corresponding optimization outcomes is conducted to highlight differences in performance and structural response.

Initial finite element setup and structural response of the 37-bar truss

As previously discussed, the finite element method (FEM) plays a central role in the developed framework, enabling accurate prediction of structural response under both geometrical and material nonlinearities. To ensure a realistic representation of structural behavior, the use of an appropriate modeling technique is essential. This section outlines the key parameters of the constructed FE model and presents the mechanical response of the initial configuration of the 37-bar truss structure, which serves as a reference for comparison with the optimized configurations. The geometry, along with the applied boundary and loading conditions, is illustrated in Fig. 9. The cross-sectional variables of the bars are defined symmetrically, reflecting the structural layout.

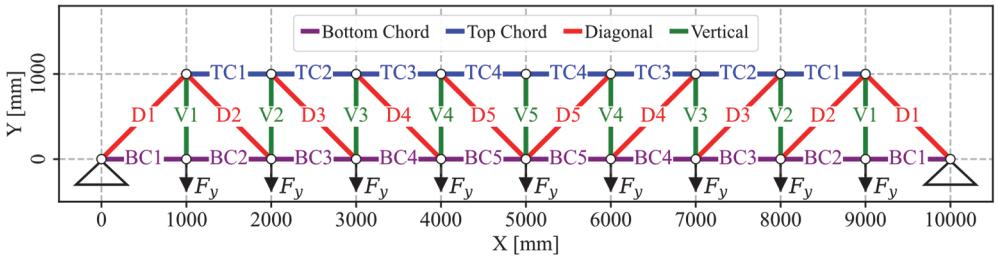

Figure 9: The layout of the 37-bar truss structure.

During the optimization process, the possible cross-sectional areas are defined in accordance with the BS EN 10210-2:2006 [23] standard, which specifies the dimensions for structural circular hollow sections (CHS) commonly used in engineering practice. Accordingly, the range of section types and corresponding geometric parameters listed in Tab. 2 are employed in the design process. For the initial configuration, the CHS 193.7/5.0 profile is applied uniformly to all bars, as illustrated in Fig. 10, with each member modeled using B31 beam elements and a general mesh size of 100mm. Consequently, the structural weight of the initial configuration is calculated as $G_{s,init} = 957.30\text{kg}$.

Section number	Section name	Specified outside diameter D (mm)	Specified wall thickness t (mm)	Cross-sectional area A (mm^2)
1	CHS 48.3/2.6	48.3	2.6	373.28
2	CHS 48.3/4.0	48.3	4.0	556.69
3	CHS 48.3/5.0	48.3	5.0	680.15
4	CHS 60.3/2.6	60.3	2.6	471.30
5	CHS 60.3/4.0	60.3	4.0	707.49
6	CHS 60.3/5.0	60.3	5.0	868.65
7	CHS 76.1/2.6	76.1	2.6	600.36
8	CHS 76.1/4.0	76.1	4.0	906.04
9	CHS 76.1/5.0	76.1	5.0	1116.84
10	CHS 88.9/3.2	88.9	3.2	704.91
11	CHS 88.9/4.0	88.9	4.0	1066.88
12	CHS 88.9/5.0	88.9	5.0	1317.90
13	CHS 101.6/3.2	101.6	3.2	989.22
14	CHS 101.6/4.0	101.6	4.0	1226.48
15	CHS 101.6/6.3	101.6	6.3	1886.18
16	CHS 114.3/3.2	114.3	3.2	1116.90
17	CHS 114.3/5.0	114.3	5.0	1716.88
18	CHS 114.3/8.0	114.3	8.0	2671.61
19	CHS 139.7/4.0	139.7	4.0	1705.26
20	CHS 139.7/6.3	139.7	6.3	2640.26
21	CHS 139.7/8.0	139.7	8.0	3309.98
22	CHS 168.3/4.0	168.3	4.0	2064.65
23	CHS 168.3/6.3	168.3	6.3	3206.31
24	CHS 168.3/8.0	168.3	8.0	4028.78
25	CHS 177.8/5.0	177.8	5.0	2714.34
26	CHS 177.8/6.3	177.8	6.3	3394.33
27	CHS 177.8/8.0	177.8	8.0	4267.54
28	CHS 193.7/5.0	193.7	5.0	2964.09
29	CHS 193.7/6.3	193.7	6.3	3709.03
30	CHS 193.7/8.0	193.7	8.0	4667.15
31	CHS 219.1/5.0	219.1	5.0	3363.07
32	CHS 219.1/8.0	219.1	8.0	5305.52

Table 2: Range of possible cross-section types used during the optimization process.

One of the most critical aspects of precise structural analysis is the accurate definition of the material's stress–strain behavior, which, in this case, corresponds to steel. This becomes even more crucial when evaluating plastic deformations. Among the available options, the quad-linear steel model proposed by Yun and Gardner [24] is adopted, as it is well-suited for numerical integration and has been calibrated against experimental results to achieve high predictive accuracy. This model comprises four distinct phases, as illustrated in Fig. 11, and is described by the following formulas:

$$\sigma = \begin{cases} E\varepsilon, \ if \ \varepsilon < \varepsilon_y \\ f_y, \ if \ \ \varepsilon_y < \varepsilon \le \varepsilon_{sh} \\ f_y + E_{sh}\left(\varepsilon - \varepsilon_{sh}\right), \ if \ \varepsilon_{sh} < \varepsilon \le C_1\varepsilon_u \\ f_{C_1\varepsilon_u} + \dfrac{f_u - f_{C_1\varepsilon_u}}{\varepsilon_u - C_1\varepsilon_u}\left(\varepsilon - C_1\varepsilon_u\right), \ if \ C_1\varepsilon_u < \varepsilon \le \varepsilon_u \end{cases} \tag{24}$$

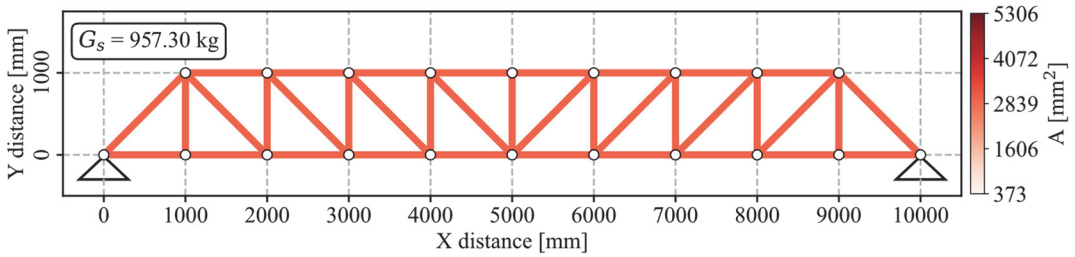

Figure 10: Distribution of cross-sectional areas assigned to each member in the initial configuration of the 37-bar truss structure.

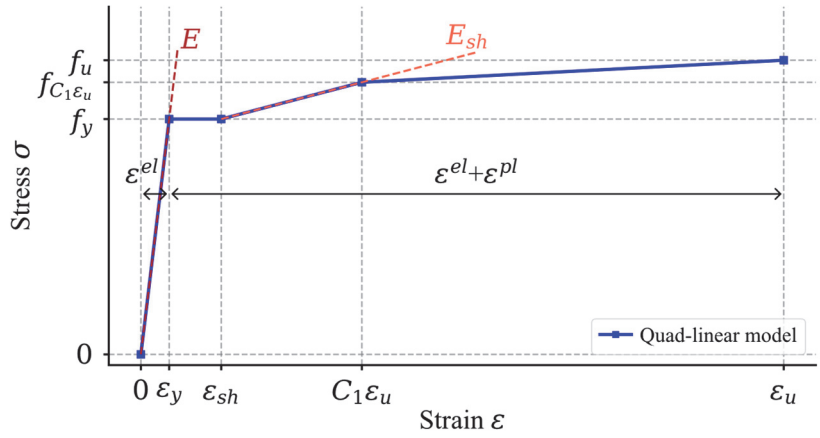

Figure 11: The illustration of the quad-linear material model of steel.

where σ denotes the stress and ε the corresponding strain. The yield stress and its associated strain are expressed as f_y and ε_y, whereas the ultimate tensile stress and strain are given by f_u and ε_u. The elastic modulus of the material is designated as E. Furthermore, the strain-hardening modulus is represented by E_{sh}, and ε_{sh} indicates the onset of strain hardening. The strain and stress corresponding to the intersection of the third segment of the idealized model with the actual stress–strain curve are denoted as $C_1\varepsilon_u$ and $f_{C_1\varepsilon_u}$, respectively, where C_1 is a material-dependent coefficient. These quantities can be evaluated using the following equations:

$$\varepsilon_u = 0.6\left(1 - \frac{f_y}{f_u}\right) \ge 0.06 \tag{25}$$

$$\varepsilon_{sh} = 0.1\frac{f_y}{f_u} - 0.055 \ \text{ and } \ 0.015 \le \varepsilon_{sh} \le 0.03 \tag{26}$$

$$C_1 = \frac{\varepsilon_{sh} + 0.25\left(\varepsilon_u - \varepsilon_{sh}\right)}{\varepsilon_u} \tag{27}$$

$$E_{sh} = \frac{f_u - f_y}{0.4\left(\varepsilon_u - \varepsilon_y\right)} \tag{28}$$

In this benchmark example, the main material properties are defined as follows: an elastic modulus $E = 200{,}000 N / mm^2$, a yield strength $f_y = 400 N / mm^2$, and an ultimate tensile strength $f_u = 550 N / mm^2$. Additionally, the material density is taken as $\rho = 7850 \text{kg} / \text{m}^3$.

The load condition of the FE model is depicted in Fig. 10, where nodal forces of $F_y = 100\text{kN}$ were applied, ultimately establishing the predefined external load vector $\boldsymbol{P}_0$. Furthermore, the boundary conditions consist of pinned supports on both sides, as illustrated in Fig. 12. Additionally, the bottom and top chord nodes were restrained in the horizontal direction, ensuring that no displacements could occur in the Z direction under the applied loading. Nevertheless, since the structural behavior was modeled using 3D B31 beam elements, out-of-plane buckling modes may still develop in compressed members.

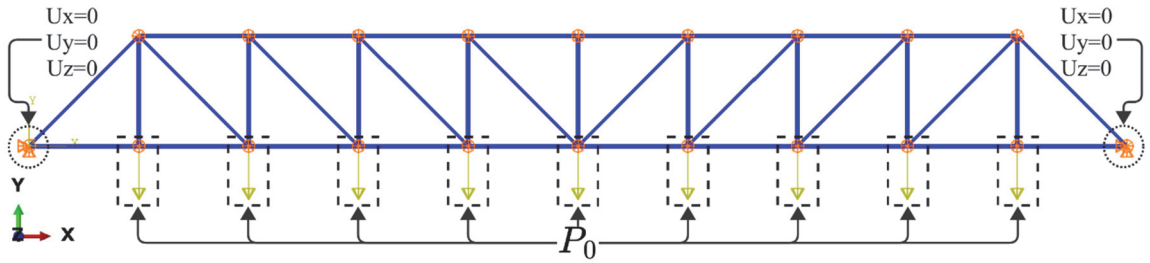

Figure 12: The developed finite element model of the 37-bar truss.

As another key aspect of the modeling, initial geometric imperfections are introduced in the initial configuration and considered throughout the subsequent optimization process. Accordingly, a linear buckling analysis (LBA) is performed, and the mode shape ϕ_1 corresponding to the first positive eigenvalue λ_1—illustrated in Fig. 13—is extracted. This eigenvalue, also referred to as the critical buckling load factor, is $\lambda_1 = \overline{\lambda} = 23.260$. As shown in Fig. 11, the imperfection primarily affects the top chord member at midspan, indicating that this region is the most sensitive to instability within the structure. As previously noted, due to the applied 3D beam elements, an out-of-plane buckling mode can be obtained, which for this structural setup can be regarded as the critical one. In this context, the imperfection amplitude is set to $\omega_1 = L / 1000$, where L denotes the length of the most critical bar.

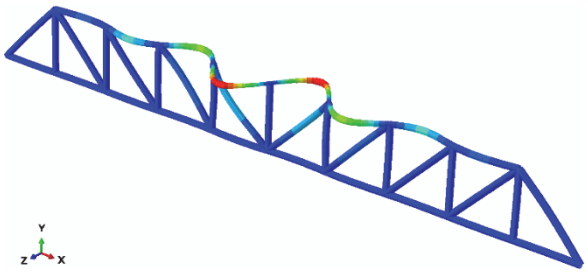

Figure 13: Buckling mode shape corresponding to the first positive eigenvalue, used to construct the initial geometric imperfection of the 37-bar truss.

The final analysis is performed using the Newton–Raphson iterative method, as mentioned earlier in this study, to capture the effects of large deformations and material nonlinearity. As previously proposed in the developed framework, plastic deformations are quantified through the complementary strain energy of the residual forces accumulated over the entire loading history. As a result, Fig. 14 presents the outcomes, showing the evolution of plastic strain energy alongside the vertical displacement of the midspan node of the bottom chord in response to the applied load levels.

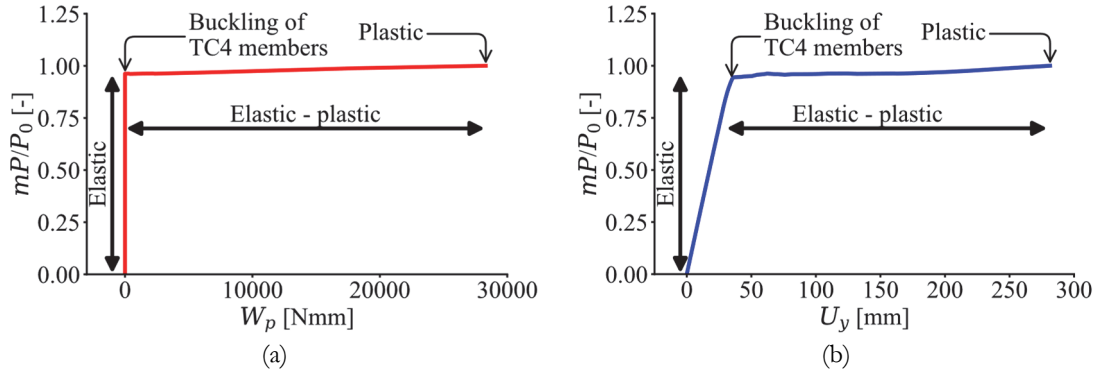

Figure 14: Results for the initial configuration of the 37-bar truss: (a) load–plastic deformation response of the entire structure; (b) load–displacement response at the midspan node of the bottom chord.

A closer examination of the presented results, as illustrated in Fig. 9, reveals that following the buckling of the most sensitive top chord members, the structure exhibits a significant loss of stiffness. As a result, both vertical displacement and plastic deformations increase substantially. However, the predefined load level is successfully reached. Furthermore, as shown in Fig. 15, the critical bars experience the largest inelastic deformations, while the remaining members predominantly remain within the elastic range under the load level. Consequently, the final value of the complementary strain energy is determined to be $W_{p,init} = 28{,}311.08\text{Nmm}$, which is adopted as the reference value W_{p0} during the optimization process. Based on this, the threshold for the elasto-plastic design scenario is defined as $W_{p,max} = 0.25W_{p0}$.

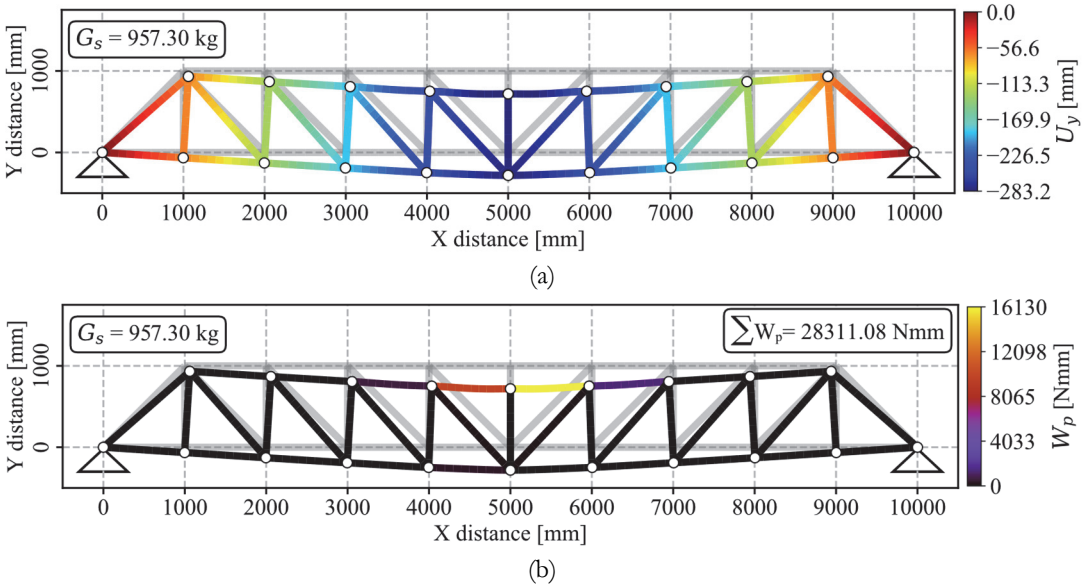

Figure 15: Distribution of (a) vertical displacements and (b) plastic deformations in the initial configuration of the 37-bar truss structure.

Comparison between optimization results of the 37-bar truss

Following the modeling principles presented in the previous section, three distinct optimization setups are conducted and compared to demonstrate the efficiency and flexibility of the proposed framework. For each setup, 10 independent optimization runs are performed to evaluate the stochastic nature of the GA and assess the reliability of the design methodology. A summary of the three configurations is provided in Tab. 3. It should be noted that the prescribed displacement limit of $U_{y,\max} = -40.00\text{mm}$ is consistent with the Eurocode recommendations, calculated as $l / 250$, where l denotes the span length of the structure.

Setup	Design scenario	W_{p0} (Nmm)	$W_{p,max}$ (Nmm)	Displacement constraint	$U_{y,max}$ (mm)	λ_{stab}	Initial geometric imperfection
E1-OP1	Elastic	–	–	NO	–	1.000	Automatically
E1-OP2	Elasto-plastic	28,311.08	7077.77	NO	–	1.000	Automatically
E1-OP3	Elasto-plastic	28,311.08	7077.77	YES	−40.00	1.000	Automatically

Table 3: Key parameters of the optimization setups for the 37-bar truss.

As a first aspect of the analysis, the convergence behavior of the three optimization setups is evaluated. As illustrated in Fig. 16, the evolution of the fitness function exhibits a similar overall trend across all configurations. In each case, a substantial drop in fitness values is observed within the initial generations, indicating rapid early improvements in the design solutions. This is followed by a stabilization phase between generations 10 and 15, where convergence slows and the population saturates around near-optimal solutions. The shaded grey regions provide a qualitative illustration of the variability across the 10 independent optimization runs, highlighting the spread and consistency of the convergence process rather than representing a defined mathematical quantity.

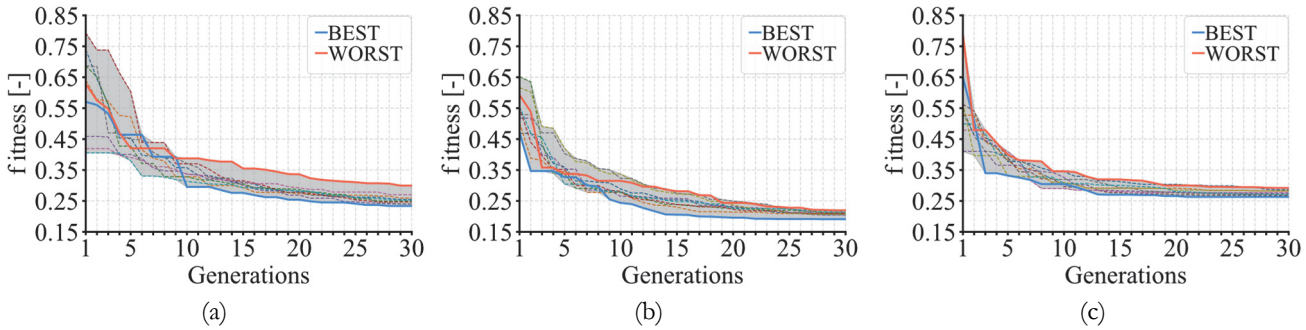

Figure 16: Fitness evolution of (a) E1-OP1, (b) E1-OP2, and (c) E1-OP3, highlighting the best and worst performing runs among 10 independent optimization processes. The shaded area represents the distribution of the remaining runs.

Corresponding to the minimum fitness values observed in each generation, the evolution of structural weight follows a similar trend across the optimization processes, as shown in Fig. 17. It is evident that E1-OP2 generally converges to a lower structural weight. This outcome results from the nature of the elasto-plastic design, in which a limited degree of plastic deformation is permitted. This flexibility enables additional material savings and guides the optimization toward lighter solutions. In contrast, E1-OP1 and E1-OP3 yield comparable final weights. This similarity arises because E1-OP3 includes a predefined maximum displacement constraint, which restricts the achievable load level and drives the optimization toward stiffer—and consequently heavier—configurations to satisfy the displacement limit.

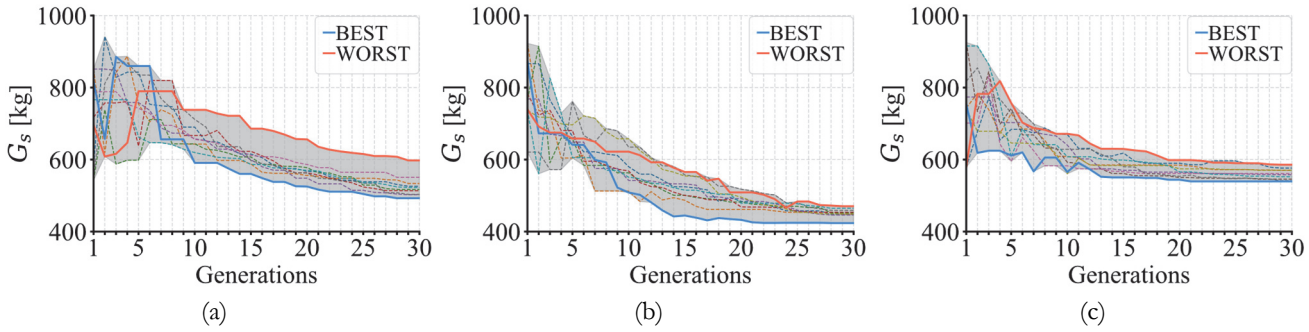

Figure 17: Structural weight evolution of (a) E1-OP1, (b) E1-OP2, and (c) E1-OP3, highlighting the best and worst performing runs among 10 independent optimization processes. The shaded area represents the distribution of the remaining runs.

In terms of the complementary strain energy of residual forces, as shown in Fig. 18, low values are generally maintained throughout the optimization process for the best-performing configurations. Under the elastic design scenario (E1-OP1),

W_p drops to zero after only 7 generations in nearly all independent runs, indicating fully elastic behavior. In contrast, for E1-OP2—where limited plastic deformations are permitted—W_p remains low but nonzero. As discussed earlier, allowing controlled plastic deformations up to a predefined threshold improves convergence and promotes material efficiency, while still maintaining minimal inelastic deformation. Conversely, the elastic design scenario imposes stricter constraints on deformation behavior, often leading to structurally conservative but less material-efficient solutions.

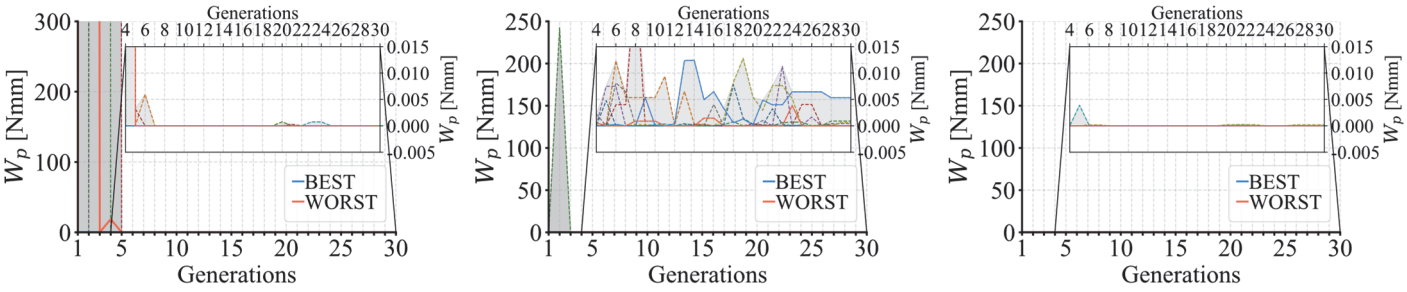

Figure 18: Complementary strain energy evolution of (a) E1-OP1, (b) E1-OP2, and (c) E1-OP3, highlighting the best and worst performing runs among 10 independent optimization processes. The shaded area represents the distribution of the remaining runs.

In terms of the load-bearing capacity associated with the best fitness values in each generation, all three optimization setups successfully achieve the predefined load level $\boldsymbol{P}_0$ in their final configurations—even in the worst-performing runs. However, as presented in Fig. 19, it is worth noting that during the early stages of optimization, only a few configurations are capable of reaching $\boldsymbol{P}_0$, highlighting the challenge of satisfying the load-carrying requirement in the absence of well-optimized configurations.

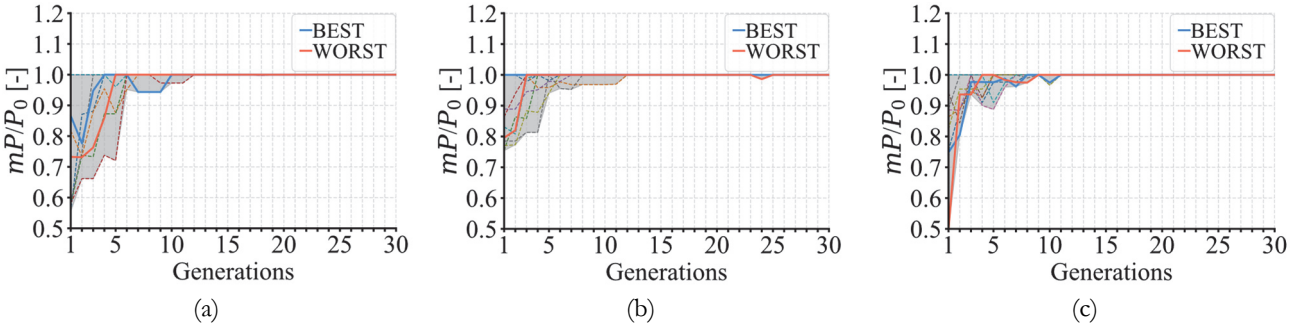

Figure 19: Load-baring evolution of (a) E1-OP1, (b) E1-OP2, and (c) E1-OP3, highlighting the best and worst performing runs among 10 independent optimization processes. The shaded area represents the distribution of the remaining runs.

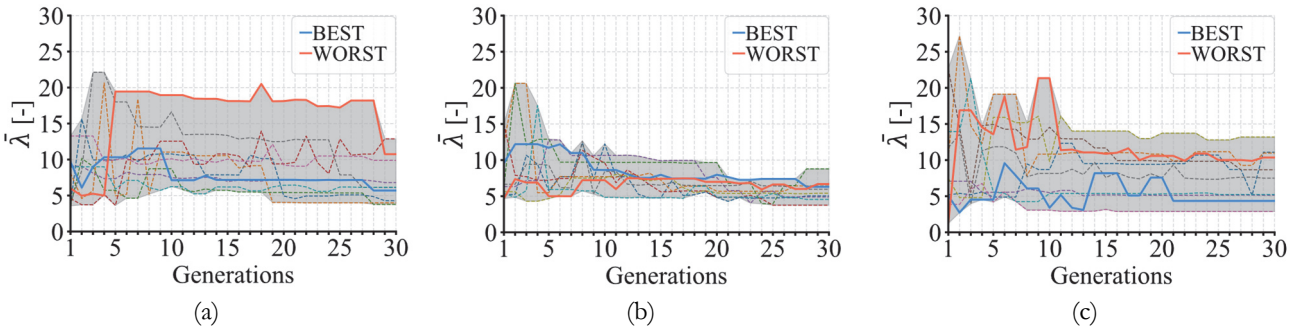

Figure 20: Critical buckling load factor evolution of (a) E1-OP1, (b) E1-OP2, and (c) E1-OP3, highlighting the best and worst performing runs among 10 independent optimization processes. The shaded area represents the distribution of the remaining runs.

As the final performance metric, the evolution of the critical buckling load factor, presented in Fig. 20, is evaluated. All three optimization setups result in relatively high buckling factors, indicating that the structure—within the defined design

domain—exhibits low sensitivity to buckling. However, in problems involving more slender structures, this parameter may become critical for achieving convergence and maintaining structural stability.

Furthermore, the results of the three optimization setups are summarized in Tabs. 4, 5, and 6, which present the mean values and standard deviations calculated from the 10 independent runs. Overall, E1-OP2 achieves the lowest average fitness value of 0.2082. Consequently—and as also reflected in the structural weight evolution—E1-OP2 yields the lowest mean structural weight of 451.54kg, while maintaining an average complementary strain energy of only 0.000725Nmm. In comparison, E1-OP1 and E1-OP3 result in higher mean weights of 525.99kg and 560.08kg, corresponding to increases of approximately 16.5% and 24.0%, respectively, relative to E1-OP2. These findings further confirm the efficiency of the elasto-plastic design scenario in enabling material-efficient solutions with minimal inelastic deformation. In addition, the highest observed standard deviation in structural weight is only 30.22kg (in the case of E1-OP1), which is relatively small considering the range of possible solutions. This demonstrates the reliability and robustness of the developed optimization framework. Finally, as shown consistently in Tabs. 4–6, all three design constraints associated with the penalty function are satisfied in every optimization run, highlighting the effectiveness of the proposed methodology in achieving compliant and high-performing structural designs.

Run	$G_s\,(\mathrm{kg})$	$W_p\,(\mathrm{Nmm})$	$m\boldsymbol{P}/\boldsymbol{P}_0\,(-)$	$\bar{\lambda}\,(-)$	*fitness*
1	525.96	0.000000	1.000	4.289	0.2545
2	533.67	0.000000	1.000	3.988	0.2593
3	517.15	0.000000	1.000	3.774	0.2490
4	513.56	0.000000	1.000	12.874	0.2467
5	502.66	0.000000	1.000	6.804	0.2399
6	597.67	0.000000	1.000	10.749	0.2995
7	550.70	0.000000	1.000	9.872	0.2700
8	503.44	0.000000	1.000	6.106	0.2404
9	492.64	0.000000	1.000	5.696	0.2336
10	522.48	0.000000	1.000	6.141	0.2523
Mean	525.99	0.000000	1.000	7.029	0.2545
Std. dev.	30.22	0.000000	0.000	3.107	0.0190

Table 4: The summary of the optimization outcomes for E1-OP1.

Run	$G_s\,(\mathrm{kg})$	$W_p\,(\mathrm{Nmm})$	$m\boldsymbol{P}/\boldsymbol{P}_0\,(-)$	$\bar{\lambda}\,(-)$	*fitness*
1	447.37	0.000000	1.000	5.043	0.2052
2	449.00	0.000004	1.000	6.431	0.2071
3	452.18	0.000893	1.000	8.787	0.2107
4	453.68	0.000000	1.000	3.754	0.2091
5	446.04	0.000418	1.000	4.898	0.2043
6	470.50	0.000000	1.000	6.686	0.2197
7	423.63	0.005305	1.000	6.302	0.1909
8	458.97	0.000000	1.000	5.964	0.2124
9	449.30	0.000627	1.000	5.418	0.2064
10	464.70	0.000000	1.000	4.554	0.2160
Mean	451.54	0.000725	1.000	5.784	0.2082
Std. dev.	12.61	0.001642	0.000	1.400	0.0078

Table 5: The summary of the optimization outcomes for E1-OP2.

Run	G_s (kg)	W_p (Nmm)	$m\boldsymbol{P}/\boldsymbol{P}_0$ (−)	$\bar{\lambda}$ (−)	*fitness*
1	576.43	0.000000	1.000	11.082	0.2862
2	569.98	0.000000	1.000	10.970	0.2821
3	539.41	0.000000	1.000	4.347	0.2629
4	585.84	0.000000	1.000	10.357	0.2921
5	557.98	0.000000	1.000	5.125	0.2746
6	545.70	0.000000	1.000	8.654	0.2692
7	561.33	0.000000	1.000	2.868	0.2767
8	541.35	0.000000	1.000	7.504	0.2669
9	570.31	0.000177	1.000	13.192	0.2823
10	552.44	0.000000	1.000	5.242	0.2711
Mean	560.08	0.000018	1.000	7.934	0.2764
Std. dev.	15.57	0.000056	0.000	3.448	0.0092

Table 6: The summary of the optimization outcomes for E1-OP3.

Parameter	Initial	E1-OP1		E1-OP2		E1-OP3	
		Best	Worst	Best	Worst	Best	Worst
A_{BC1}	CHS193.7/5.0	CHS76.1/4.0	CHS76.1/5.0	CHS101.6/3.2	CHS76.1/4.0	CHS88.9/2.6	CHS219.1/5.0
A_{BC2}	CHS193.7/5.0	CHS60.3/5.0	CHS168.3/6.3	CHS88.9/4.0	CHS88.9/2.6	CHS48.3/5.0	CHS76.1/5.0
A_{BC3}	CHS193.7/5.0	CHS88.9/4.0	CHS101.6/3.2	CHS60.3/2.6	CHS48.3/4.0	CHS60.3/2.6	CHS60.3/4.0
A_{BC4}	CHS193.7/5.0	CHS88.9/4.0	CHS76.1/5.0	CHS76.1/2.6	CHS76.1/5.0	CHS139.7/4.0	CHS60.3/4.0
A_{BC5}	CHS193.7/5.0	CHS114.3/5.0	CHS76.1/5.0	CHS88.9/4.0	CHS101.6/6.3	CHS168.3/4.0	CHS114.3/3.2
A_{TC1}	CHS193.7/5.0	CHS177.8/5.0	CHS168.3/6.3	CHS168.3/4.0	CHS177.8/5.0	CHS193.7/5.0	CHS193.7/6.3
A_{TC2}	CHS193.7/5.0	CHS168.3/6.3	CHS139.7/8.0	CHS193.7/5.0	CHS168.3/6.3	CHS219.1/5.0	CHS219.1/5.0
A_{TC3}	CHS193.7/5.0	CHS177.8/6.3	CHS168.3/8.0	CHS139.7/8.0	CHS177.8/6.3	CHS168.3/8.0	CHS219.1/5.0
A_{TC4}	CHS193.7/5.0	CHS193.7/6.3	CHS168.3/8.0	CHS219.1/5.0	CHS177.8/6.3	CHS193.7/8.0	CHS219.1/8.0
A_{D1}	CHS193.7/5.0	CHS168.3/4.0	CHS177.8/5.0	CHS114.3/5.0	CHS139.7/4.0	CHS177.8/5.0	CHS168.3/6.3
A_{D2}	CHS193.7/5.0	CHS88.9/5.0	CHS114.3/3.2	CHS114.3/5.0	CHS101.6/4.0	CHS101.6/4.0	CHS139.7/4.0
A_{D3}	CHS193.7/5.0	CHS76.1/5.0	CHS114.3/3.2	CHS76.1/4.0	CHS168.3/4.0	CHS139.7/4.0	CHS101.6/3.2
A_{D4}	CHS193.7/5.0	CHS88.9/2.6	CHS48.3/4.0	CHS76.1/2.6	CHS60.3/4.0	CHS101.6/3.2	CHS88.9/4.0
A_{D5}	CHS193.7/5.0	CHS76.1/4.0	CHS48.3/2.6	CHS60.3/2.6	CHS48.3/2.6	CHS88.9/2.6	CHS48.3/2.6
A_{V1}	CHS193.7/5.0	CHS76.1/2.6	CHS88.9/4.0	CHS48.3/2.6	CHS48.3/4.0	CHS48.3/2.6	CHS48.3/2.6
A_{V2}	CHS193.7/5.0	CHS76.1/5.0	CHS177.8/6.3	CHS76.1/5.0	CHS60.3/5.0	CHS60.3/4.0	CHS76.1/4.0
A_{V3}	CHS193.7/5.0	CHS114.3/3.2	CHS114.3/3.2	CHS101.6/3.2	CHS88.9/2.6	CHS101.6/4.0	CHS76.1/4.0
A_{V4}	CHS193.7/5.0	CHS88.9/4.0	CHS114.3/5.0	CHS76.1/2.6	CHS60.3/5.0	CHS48.3/5.0	CHS114.3/5.0
A_{V5}	CHS193.7/5.0	CHS48.3/2.6	CHS48.3/5.0	CHS60.3/4.0	CHS101.6/3.2	CHS48.3/5.0	CHS48.3/4.0
G_s	957.30kg	492.64kg	597.67kg	423.63kg	470.50kg	539.41kg	585.84kg
$G_s / G_{s,init}$	1.000	0.515	0.624	0.443	0.491	0.563	0.612
$\max_y \lvert U_y \rvert$	−283.2mm	−51.63mm	−47.29mm	−60.64mm	−52.70mm	−40.03mm	−40.19mm

Table 7: Comparison of the initial configuration with the best- and worst-performing solutions from E1-OP1, E1-OP2, and E1-OP3.

To complement the comparison, Tab. 7 presents the cross-section types of the best- and worst-performing solutions, alongside their corresponding weight and displacement results. Notably, even the least favorable outcomes in each case lead to a substantial reduction in weight compared to the initial configuration, while fully satisfying all structural criteria defined

by the respective design settings. Specifically, the worst solutions of E1-OP1, E1-OP2, and E1-OP3 achieve approximately 37.6%, 50.9%, and 38.8% weight savings, while the best-performing designs reach 48.5%, 55.7%, and 43.7%, respectively—demonstrating the overall robustness of the proposed optimization framework. Regarding maximum vertical displacement, all configurations outperform the initial setup. In E1-OP3, where a displacement constraint is enforced, the final solution remains within the prescribed limit, with only a negligible exceedance—well within acceptable engineering tolerances. These results emphasize the framework's capability to deliver both material-efficient and regulation-compliant designs, even under suboptimal optimization outcomes.

To visually support the comparison, the cross-section distributions of these configurations are illustrated in Fig. 21. As anticipated, the most critical members—specifically the top chords at midspan and the diagonals near the supports—are assigned the largest cross-sectional areas. This outcome further demonstrates that the applied penalty formulations effectively guide the optimization toward reinforcing structurally sensitive regions, while enabling material savings in less critical members.

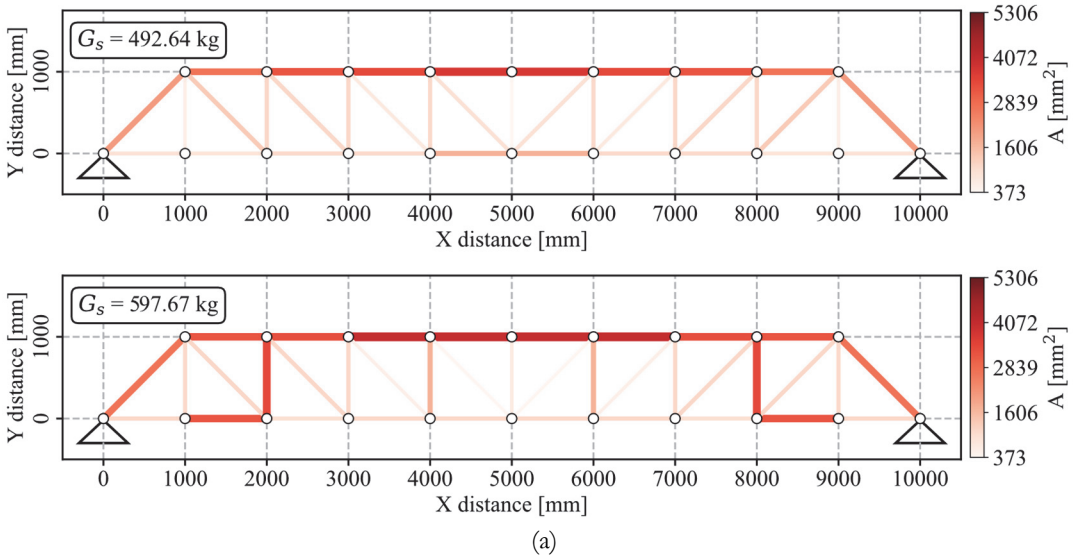

(a)

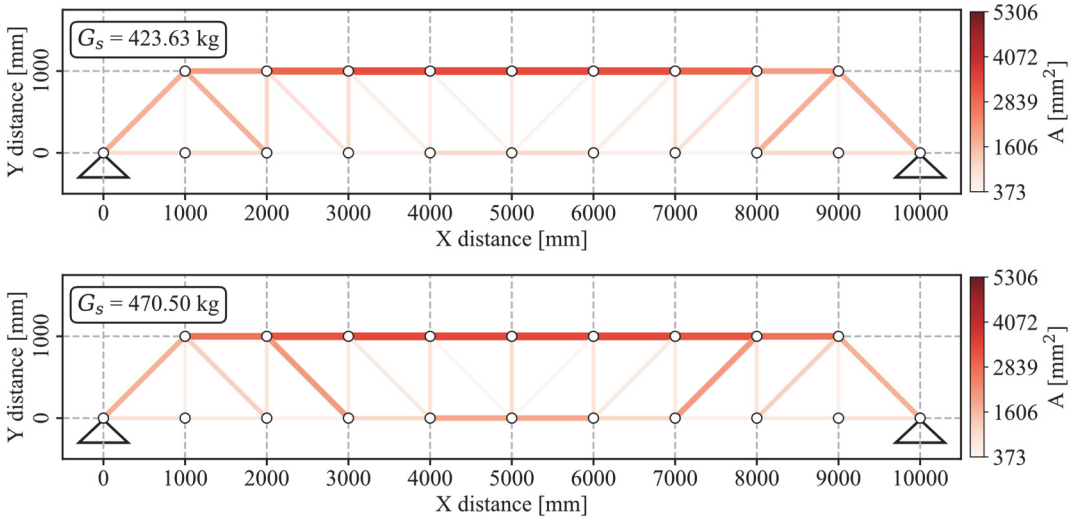

(b)

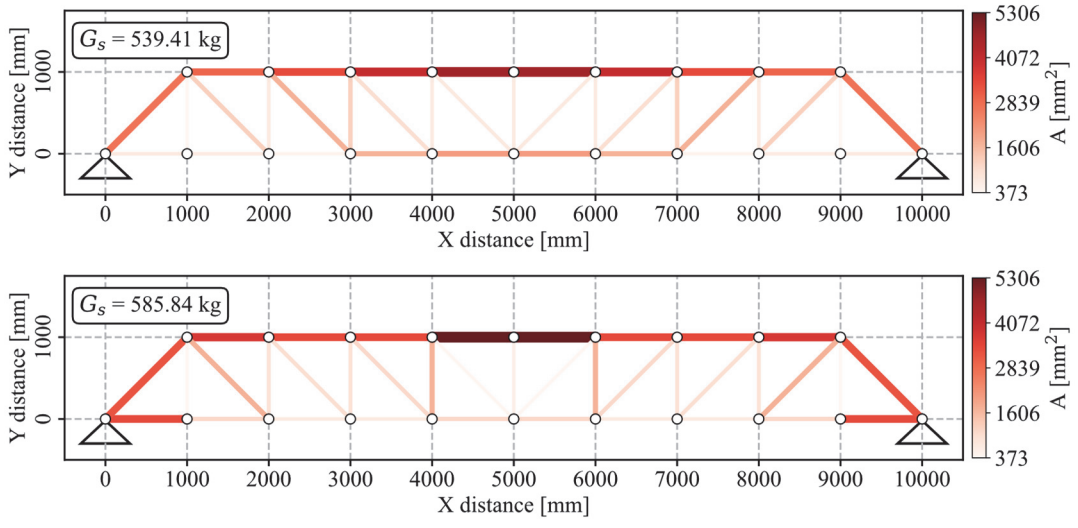

(c)

Figure 21: Cross-sectional area distribution for the best and worst configurations of (a) E1-OP1, (b) E1-OP2, and (c) E1-OP3 in the 37-bar truss.

BENCHMARK NUMERICAL EXAMPLE: 25-BAR SPACE TRUSS

This section presents the second numerical example, the well-known 25-bar truss structure. Two elasto-plastic optimization setups were conducted—one with a displacement constraint and one without—and the resulting solutions were compared to evaluate the effectiveness of the proposed methodology.

Initial finite element setup and structural response of the 25-bar truss

Consistent with the operation of the proposed framework, the FE model of the 25-bar truss was constructed using the same modelling technique as in the first numerical example. Accordingly, this section highlights the key differences in the structure. In this benchmark, the members are divided into eight design groups, each governed by a common cross-sectional area variable, as shown in Fig. 22(a). In this case, the same sections listed in Tab. 2 are considered as design variables. The initial setup was constructed as follows: groups 1-3 are assigned CHS 48.3/4.0, and groups 4-8 are assigned CHS 88.9/4.0. Consequently, the cross-sectional area distribution of the structure is shown in Fig. 22(b). This initial setup—including its structural weight $G_{s,init} = 599.34\text{kg}$ assuming material density $\rho = 7850\text{kg} / \text{m}^3$—serves as the reference configuration for the optimization results presented in the subsequent section.

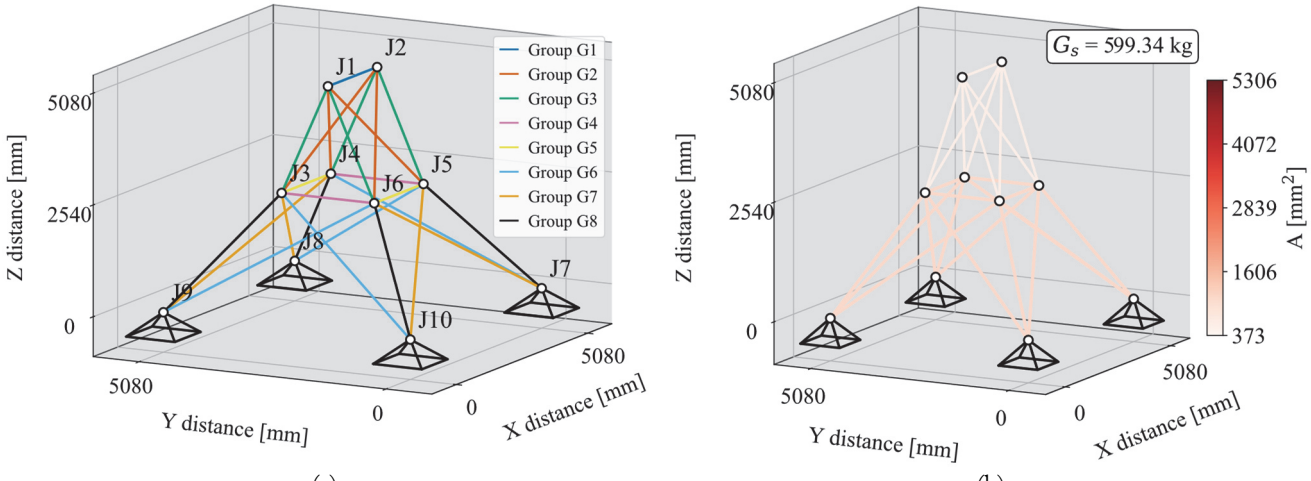

(a) (b)

Figure 22: The 25-bar truss: (a) structural layout; (b) distribution of cross-sectional areas assigned to each member in the initial configuration.

As in the previous example, the FE model of the 25-bar truss is developed using B31 beam elements with a uniform 100mm mesh size and the same quad-linear constitutive model for steel. The primary material properties are as follows: elastic modulus $E = 207{,}000\text{N}/\text{mm}^2$, yield strength . $f_y = 240\text{N}/\text{mm}^2$., and ultimate tensile strength $f_u = 360\text{N}/\text{mm}^2$.

The load and boundary conditions are prescribed as shown in Fig. 23(a), with nodal forces specified in Tab. 8. As in the previous example, the LBA is first carried out to obtain the critical mode shape used to define the initial geometric imperfection. The analysis yields a critical buckling load factor $\lambda_1 = \bar{\lambda} = 0.388$, and the corresponding mode shape is shown in Fig. 23(b). It should be noted that this configuration does not satisfy the predefined stability criterion of $\bar{\lambda} \geq 1.000$, introduced in the previous benchmark optimization and adopted herein as well, as further detailed in the next section. Consistent with the first example, the length L of the most critical member is used to scale the imperfection, with amplitude $\omega_1 = L/1000$.

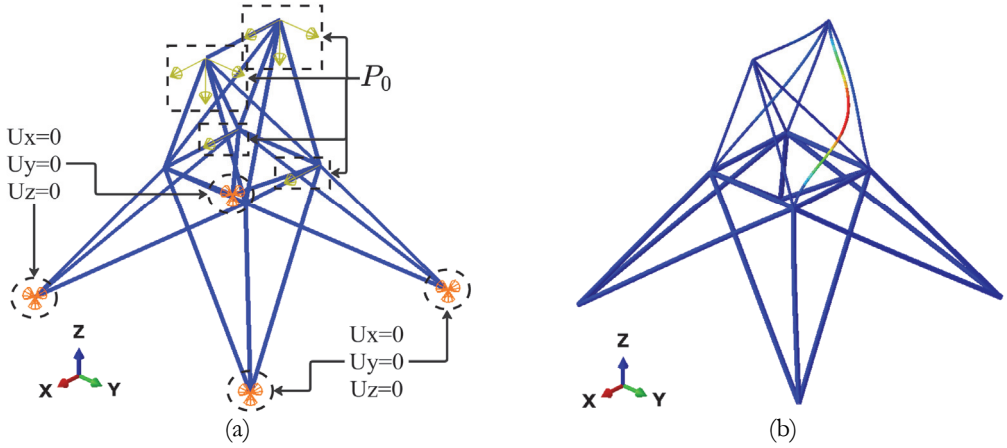

Figure 23: The 25-bar truss: (a) the developed FE model; (b) buckling mode shape associated with the first positive eigenvalue, used to define the initial geometric imperfection.

Node	Force (kN)		
	P_x	P_y	P_z
J1	80.0	120.0	−30.0
J2	60.0	100.0	−30.0
J4	30.0	0.0	0.0
J5	30.0	0.0	0.0

Table 8: The nodal loading configuration of the 25-bar space truss.

To precisely determine the complementary plastic work W_p, the GAMNA is also conducted for this benchmark using the Newton–Raphson scheme. The results are summarized in Fig. 23, showing the load–plastic deformation response and the displacement in the Y-direction of node J2 at the top of the structure. It can be observed that, following the buckling of the group 2 members—consistent with the prescribed geometric imperfection—no further increase in load-carrying capacity occurs. Consequently, only approximately 61.5% of the predefined load level $\boldsymbol{P}_0$ is achieved during the loading process. In the post-buckling regime, prior to the complete loss of stability, only moderate plastic deformation develops; therefore, the complementary plastic work is evaluated as $W_{p,init} = 43.40\text{Nmm}$. As in the previous benchmark, this value is adopted as the reference W_{p0} for the optimization, and the elasto-plastic limit is fixed at $W_{p,max} = 0.25W_{p0}$.

Comparison between optimization results of the 25-bar truss

After the principal characteristics of the 25-bar truss have been presented and the initial configuration evaluated, two optimization setups are introduced in this section. To characterize the stochastic behavior of the GA and assess methodological reliability, 5 independent runs are performed for each setup. The configurations are summarized in Tab. 9,

which were compared in the following. In this example as well, the prescribed maximum displacement limit of $U_{y,\max} = 12.70\text{mm}$ is defined in accordance with Eurocode standards, considering a total structural height of $H = 5080\text{mm}$ and the corresponding serviceability limit of $H / 400$.

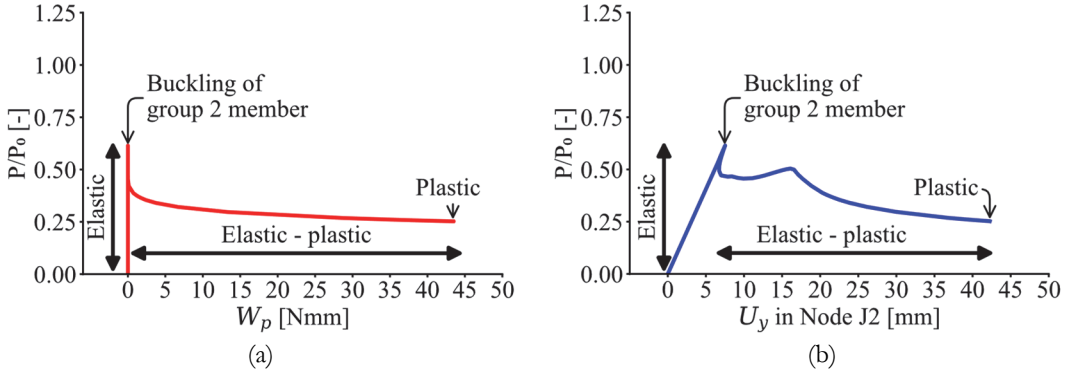

Figure 24: Results for the initial configuration of the 25-bar truss: (a) load–plastic deformation response of the entire structure; (b) load–displacement response at node J2.

Setup	Design scenario	W_{p0} (Nmm)	$W_{p,max}$ (Nmm)	Displacement constraint	$U_{y,max}$ (mm)	λ_{stab}	Initial geometric imperfection
E2-OP2	Elasto-plastic	43.40	10.85	NO	–	1.000	Automatically
E2-OP3	Elasto-plastic	43.40	10.85	YES	12.70	1.000	Automatically

Table 9: Key parameters of the optimization setups for the 25-bar truss.

As a first step in the analysis, Fig. 25 compares the convergence histories of the generation-wise minimum fitness for E2-OP1 and E2-OP2. In both cases, the sequence drops sharply in the early generations and then transitions to a slower, monotonic approach to a plateau. The gray band—the gap between the best and worst individuals—visually indicates the population variance, as in the previous example. By the final generations, both setups reach nearly identical fitness levels, demonstrating comparable convergence behavior and overall performance.

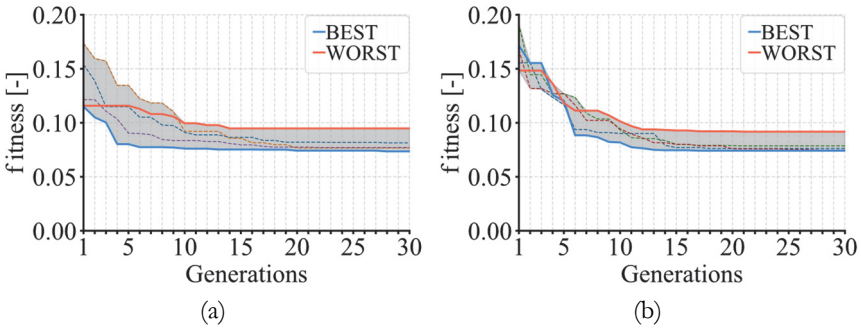

Figure 25: Fitness evolution of (a) E2-OP1 and (b) E2-OP3, highlighting the best and worst performing runs among 5 independent optimization processes. The shaded area represents the distribution of the remaining runs.

Consistent with the minimum-fitness history, the generation-wise structural weight follows a similar trend, as shown in Fig. 26. This suggests that, near convergence, the weight component dominates the objective function. The final structural weights for E2-OP1 and E2-OP2 are essentially identical, indicating comparable solutions across the two setups.

In this numerical example as well, the complementary plastic work of the residual forces W_p for the best-fitness solutions remains small, although not strictly zero in every case, as shown in Fig. 27. Moreover, all final designs across the runs satisfy the prescribed limit $W_{p,max}$, demonstrating that the proposed formulation effectively controls plastic deformations.

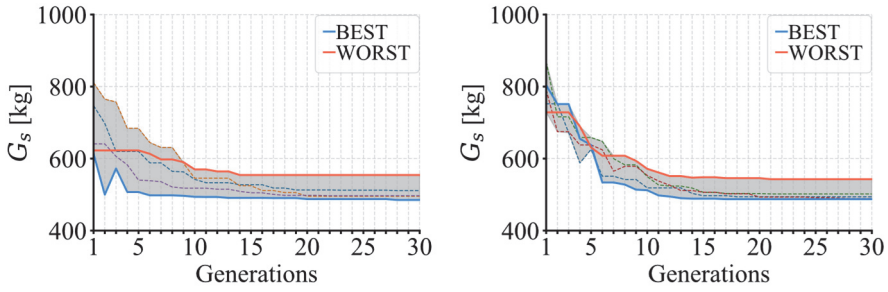

Figure 26: Structural weight evolution of (a) E2-OP1 and (b) E2-OP3, highlighting the best and worst performing runs among 5 independent optimization processes. The shaded area represents the distribution of the remaining runs.

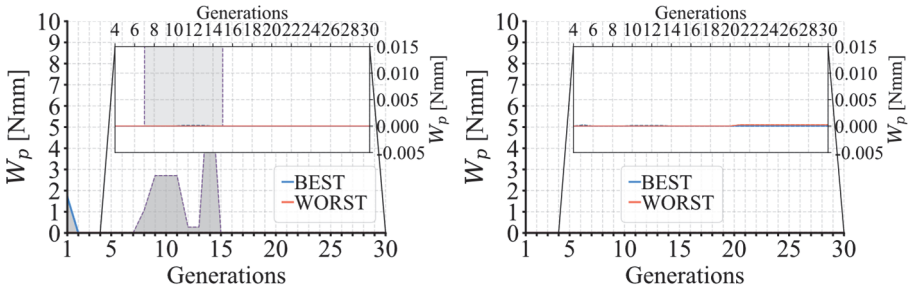

Figure 27: Complementary strain energy evolution of (a) E2-OP1 and (b) E2-OP3, highlighting the best and worst performing runs among 5 independent optimization processes. The shaded area represents the distribution of the remaining runs.

For the attained load levels evaluated at the best-fitness designs, both E2-OP1 and E2-OP2 reach the prescribed target P_0 in all runs. Consequently, the proposed framework reliably achieves the required load-bearing capacity under the stated conditions.

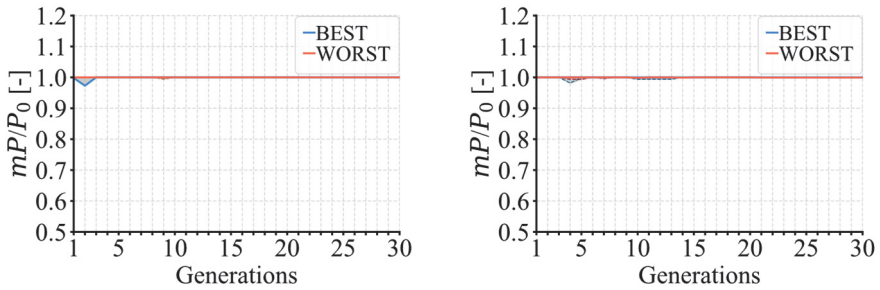

Figure 28: Load-baring evolution of (a) E2-OP1 and (b) E2-OP3, highlighting the best and worst performing runs among 5 independent optimization processes. The shaded area represents the distribution of the remaining runs.

In the case of the critical buckling load factors, Fig. 29 shows that, compared to the previous 37-bar example, generally lower values were obtained. Nevertheless, for all best-performing solutions based on fitness across the individual runs—including both E2-OP1 and E2-OP2—the proposed framework achieved critical buckling load factors $\bar{\lambda}$ exceeding the predefined stability threshold of $\lambda_{stab} = 1.000$.

As observed in Figs. 25–29, both optimization setups, E2-OP1 and E2-OP2, yielded similar fitness values and corresponding structural properties, as further detailed in Tab. 10. Remarkably, all final solutions satisfied the structural criteria enforced through the penalty functions: the complementary strain energy of residual forces W_p remained below the

predefined limit $W_{p,\max}$, the target load-bearing capacity $\boldsymbol{P}_0$ was achieved, and the critical buckling load factor exceeded unity ($\bar{\lambda} > 1.000$) in all cases, while the material usage was effectively minimized. The results obtained provide additional confirmation of the reliability and robustness of the developed optimization framework.

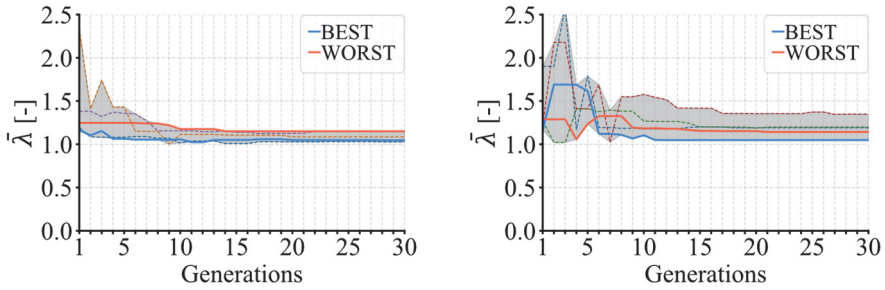

Figure 29: Critical buckling load factor evolution of (a) E2-OP1 and (b) E2-OP3, highlighting the best and worst performing runs among 5 independent optimization processes. The shaded area represents the distribution of the remaining runs.

Run	E2-OP1					E2-OP2				
	G_s (kg)	W_p (Nmm	$m\boldsymbol{P}/\boldsymbol{P}_0$ (−)	$\bar{\lambda}$ (−)	*fitness*	G_s (kg)	W_p (Nmm)	$m\boldsymbol{P}/\boldsymbol{P}_0$ (−)	$\bar{\lambda}$ (−)	*fitness*
1	510.87	0.00000	1.000	1.027	0.0814	494.06	0.00000	1.000	1.190	0.0762
2	495.47	0.00000	1.000	1.085	0.0767	542.81	0.00022	1.000	1.142	0.0918
3	485.14	0.00000	1.000	1.047	0.0735	501.77	0.00000	1.000	1.199	0.0786
4	554.47	0.00000	1.000	1.150	0.0948	489.08	0.00000	1.000	1.348	0.0747
5	496.81	0.00000	1.000	1.147	0.0771	487.25	0.00000	1.000	1.048	0.0741
Mean	508.55	0.00000	1.000	1.091	0.0807	502.99	0.00004	1.000	1.185	0.0791
Std. dev.	27.25	0.00000	0.000	0.057	0.0084	22.96	0.00010	0.000	0.109	0.0073

Table 10: The summary of the optimization outcomes for E2-OP1 and E2-OP2.

Parameter	Initial	E2-OP1		E2-OP2	
		Best	Worst	Best	Worst
A_{G1}	CHS48.3/4.0	CHS48.3/2.6	CHS48.3/2.6	CHS48.3/2.6	CHS48.3/2.6
A_{G2}	CHS48.3/4.0	CHS60.3/5.0	CHS60.3/5.0	CHS60.3/5.0	CHS60.3/5.0
A_{G3}	CHS48.3/4.0	CHS76.1/4.0	CHS76.1/4.0	CHS76.1/4.0	CHS76.1/4.0
A_{G4}	CHS88.9/4.0	CHS48.3/2.6	CHS48.3/2.6	CHS48.3/2.6	CHS48.3/2.6
A_{G5}	CHS88.9/4.0	CHS101.6/3.2	CHS101.6/3.2	CHS101.6/3.2	CHS101.6/3.2
A_{G6}	CHS88.9/4.0	CHS76.1/2.6	CHS76.1/2.6	CHS76.1/2.6	CHS76.1/2.6
A_{G7}	CHS88.9/4.0	CHS48.3/2.6	CHS48.3/2.6	CHS48.3/2.6	CHS48.3/2.6
A_{G8}	CHS88.9/4.0	CHS101.6/4.0	CHS101.6/4.0	CHS101.6/4.0	CHS101.6/4.0
G_s	599.34kg	485.14kg	554.47kg	487.25kg	542.81kg
$G_s / G_{s,init}$	1.000	0.809	0.925	0.813	0.906
$\max_y \lvert U_y \rvert$	42.3mm	10.9mm	8.6mm	10.7*mm*	10.9mm

Table 11: Comparison of the initial configuration with the best- and worst-performing solutions from E2-OP1 and E2-OP2.

In addition to the previously discussed results, Tab. 11 presents the cross-sectional types corresponding to the best- and worst-performing cases for both optimization setups, E2-OP1 and E2-OP2, together with the reference configuration. Relative to the latter, a total weight reduction of approximately 7.5% was obtained for the least efficient optimized case, while the best-performing design achieved a 19.1% decrease. Notably, as mentioned earlier, all structural requirements were fulfilled in the optimized designs. In contrast, the initial configuration failed to reach the predefined load-bearing capacity—attaining only 61.5% of $\boldsymbol{P}_0$—and did not satisfy the stability criterion ($\lambda = 0.388 < 1.000$). Consequently, the reference setup exhibited inferior performance despite its greater material usage. These outcomes further highlight the effectiveness of the proposed automated optimization framework in producing lightweight yet structurally compliant designs. The corresponding cross-sectional area distributions for the best and worst configurations obtained in both E2-OP1 and E2-OP2 are illustrated in Fig. 30.

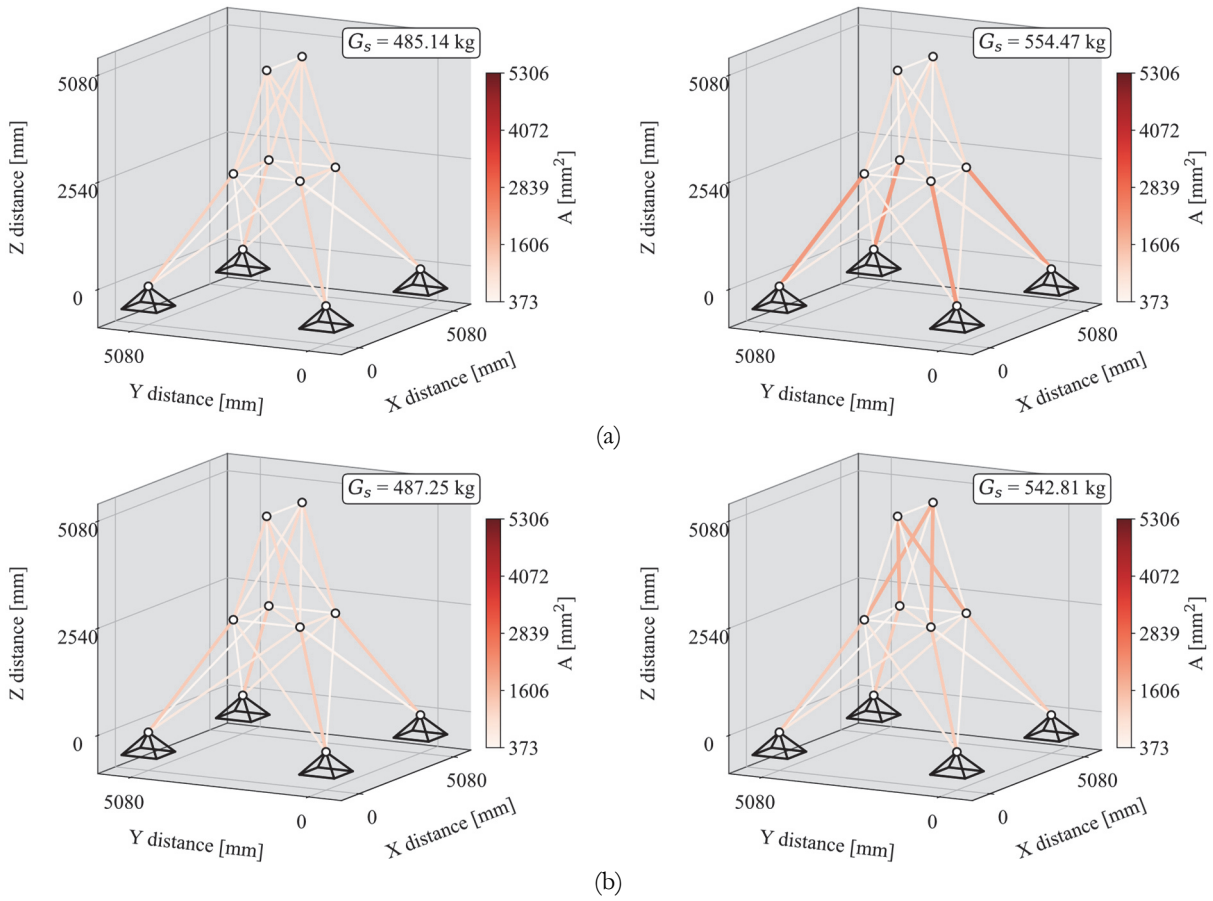

Figure 30: Cross-sectional area distribution for the best and worst configurations of (a) E2-OP1, and (b) E2-OP2 in the 25-bar truss.

Furthermore, as shown in Tab. 11, both the best and worst configurations obtained in E2-OP1 satisfied the serviceability requirement defined by the displacement limit ($\max_y |U_y| < U_{\max}$), even though this constraint was not active during the optimization process. This result can be attributed to the definition of the design space, which inherently promotes relatively stiff structural configurations compared to the prescribed displacement threshold ($U_{\max} = 12.70\text{mm}$). Consequently, the displacement constraint exerted no significant influence on the optimization outcome, explaining the close similarity observed between the results of E2-OP1 and E2-OP2.

CONCLUSION

In this paper, a developed framework is presented for the elastic and elasto-plastic design of truss structures, employing the complementary strain energy of residual forces as a key parameter to quantify inelastic deformations. The proposed methodology is specifically devised to automatically minimize the cross-sectional areas of bar members while ensuring that all structural criteria are satisfied for a safe and feasible solution. This is achieved through the implementation of a relatively complex fitness function, which—in addition to structural weight—includes penalty terms for plastic deformations, load-bearing capacity, and global stability. A displacement constraint is also integrated to account for serviceability requirements. Furthermore, the framework is capable of incorporating plastic material behavior, large deformation effects, and initial geometric imperfections, thereby enabling highly accurate and realistic structural designs. The entire approach is implemented using the ABAQUS finite element software in conjunction with the PYTHON programming language.

To demonstrate the efficiency, flexibility, and potential of the proposed design strategy, two well-known benchmark structures—the 37-bar and 25-bar trusses—are investigated. For the former, three distinct optimization setups are examined: E1-OP1, based on purely elastic design criteria; E1-OP2, incorporating elasto-plastic analysis by allowing limited inelastic deformations up to a predefined threshold; and E1-OP3, which extends E1-OP2 by introducing a displacement constraint. In the case of the 25-bar truss, two elasto-plastic design scenarios are evaluated: without (E2-OP1) and with (E2-OP2) displacement constraint. Each setup is executed through multiple independent optimization runs to account for the stochastic nature of the genetic algorithm and to ensure a reliable assessment of performance. The key findings are summarized below:

1. In all optimization setups, substantial material savings were achieved while fully satisfying the structural criteria defined for each design scenario. For the 37-bar truss, E1-OP1 led to a weight reduction of approximately 48.5%, E1-OP2 reached 55.7%, and E1-OP3 resulted in 43.7% savings relative to the initial configuration, confirming the framework's efficiency across varying design objectives. Similarly, for the 25-bar truss, the elasto-plastic optimization without a displacement constraint (E2-OP1) achieved a weight reduction of 19.1%, while the setup incorporating the serviceability criterion (E2-OP2) attained 18.7% savings compared to the reference configuration. In both benchmarks, all structural performance requirements—including load-bearing capacity, stability, and plastic deformation limits—were satisfied, further confirming the robustness and versatility of the proposed optimization framework across different structural configurations.
2. The elasto-plastic design approach without displacement constraint, applied in E1-OP2, results in greater material efficiency compared to the fully elastic scenario in E1-OP1, while still maintaining tight control over inelastic deformations. Within the defined design domain of the 37-bar truss, this strategy achieves an average weight reduction of 16.5%, with plastic deformation remaining negligible. Allowing limited plasticity also enhances convergence, as it permits the identification of lighter configurations capable of tolerating moderate inelastic effects without compromising structural safety.
3. The integration of a displacement constraint further enhances the framework's versatility by ensuring that the prescribed serviceability limit is only marginally exceeded, while still achieving weight minimization and fulfilling all structural performance requirements, as demonstrated in the E1-OP3 results. This constraint leads to inherently stiffer configurations and results in an average weight increase of approximately 24.0% compared to the best-performing E1-OP2 solutions, which operate without displacement limitations. In the case of the 25-bar truss, both optimization setups—E2-OP1 and E2-OP2—satisfied the prescribed displacement limit, even though it was not explicitly active in the former. This favorable outcome demonstrates that the defined design space inherently promotes sufficiently stiff structural configurations, ensuring compliance with serviceability requirements without additional constraints. Consequently, the displacement limitation exerted minimal influence on the optimization process. Nevertheless, the framework retains the flexibility to impose stricter serviceability limits by adjusting the displacement threshold when necessary, further highlighting the overall robustness, adaptability, and effectiveness of the proposed optimization methodology.

In conclusion, the proposed framework facilitates an advanced, automated design process capable of generating material-efficient and structurally robust truss configurations. These results underscore the potential of advanced optimization tools to enhance structural engineering practice through more intelligent, performance-driven design methodologies.

ACKNOWLEDGEMENTS

This project was implemented with the support provided by the Ministry of Culture and Innovation of Hungary from the National Research, Development and Innovation Fund, financed under the University Research Scholarship Program EKÖP-2024-06.

REFERENCES

[1] Piroglu, F., Ozakgul, K., Iskender, H., Trabzon, L., Kahya, C. (2014). Site investigation of damages occurred in a steel space truss roof structure due to ponding. Eng Fail Anal 36, pp. 301–313, DOI: https://doi.org/10.1016/j.engfailanal.2013.10.018.

[2] Zheng, H.D., Fan, J. (2018). Analysis of the progressive collapse of space truss structures during earthquakes based on a physical theory hysteretic model. Thin-Walled Structures 123, pp. 70–81, DOI: https://doi.org/10.1016/j.tws.2017.10.051.

[3] Warner, T.K. (1960). General Theorems for Elastic-plastic Solids. In: Sneddon, I.N., Hill, R., (Eds.), Progress of Solid Mechanics, North-Holland Publisher Company, pp. 167–221.

[4] Capurso, M. (1974). A displacement bounding principle in shakedown of structures subjected to cyclic loads. Int J Solids Struct 10(1), pp. 77–92, DOI: https://doi.org/10.1016/0020-7683(74)90102-4.

[5] Maier, G., Grierson, D.E., Best, M.J. (1977). Mathematical programming methods for deformation analysis at plastic collapse. Comput Struct 7(5), pp. 599–612, DOI: https://doi.org/10.1016/0045-7949(77)90002-5.

[6] Kaliszky, S. (1996). Elastoplastic analysis with limited plastic deformations and displacements. Mechanics of Structures and Machines 24(1), pp. 39–50, DOI: https://doi.org/10.1080/08905459608905254.

[7] Kaliszky, S., Lógó, J. (1997). Optimal plastic limit and shake-down design of bar structures with constraints on plastic deformation. Eng Struct 19(1), pp. 19–27.

[8] Kaliszky, S., Lógó, J. (1999). Optimal strengthening of elasto-plastic trusses with plastic deformation and stability constraints. Structural Optimization 18, pp. 296–299.

[9] Movahedi Rad, M., Habashneh, M., Lógó, J. (2023). Reliability based bi-directional evolutionary topology optimization of geometric and material nonlinear analysis with imperfections. Comput Struct 287, DOI: https://doi.org/10.1016/j.compstruc.2023.107120.

[10] Silva, W.T.M., Ribeiro, K.B., Portela, A. (2024). Nonlinear analysis of spatial trusses with different strain measures and compressible solid. Int J Non Linear Mech 167, DOI: https://doi.org/10.1016/j.ijnonlinmec.2024.104907.

[11] Noor, A.K., Peters, J.M. (1980). Nonlinear dynamic analysis of space trusses. Comput Methods Appl Mech Eng 21(2), pp. 131–151, DOI: https://doi.org/10.1016/0045-7825(80)90027-4.

[12] Kim, N.-H. (2015). Introduction to Nonlinear Finite Element Analysis. Springer US, New York, NY.

[13] Peng, Y., Li, Z., Kamel, M.M.A. (2021). Geometrical nonlinear problems of truss beam by base force element method. Int J Numer Methods Eng 122(18), pp. 4793–824, DOI: https://doi.org/10.1002/nme.6746.

[14] Saka, M.P., Ulker, M. (1992). Optimum design of geometrically nonlinear space trusses. Comput Struct 42(3), pp. 289–299, DOI: https://doi.org/10.1016/0045-7949(92)90025-U.

[15] Madah, H., Amir, O. (2017). Truss optimization with buckling considerations using geometrically nonlinear beam modeling. Comput Struct 192, pp. 233–247, DOI: https://doi.org/10.1016/j.compstruc.2017.07.023.

[16] Li, L., Khandelwal, K. (2017). Topology optimization of geometrically nonlinear trusses with spurious eigenmodes control. Eng Struct 131, pp. 324–344, DOI: https://doi.org/10.1016/j.engstruct.2016.11.001.

[17] Truong, V.H., Kim, S.E. (2018). Reliability-based design optimization of nonlinear inelastic trusses using improved differential evolution algorithm. Advances in Engineering Software 121, pp. 59–74, DOI: https://doi.org/10.1016/j.advengsoft.2018.03.006.

[18] Truong, V.H., Tangaramvong, S., Papazafeiropoulos, G. (2024). An efficient LightGBM-based differential evolution method for nonlinear inelastic truss optimization. Expert Syst Appl 237, DOI: https://doi.org/10.1016/j.eswa.2023.121530.

[19] Truong, V.H., Pham, H.A., Tangaramvong, S. (2025). An efficient method for nonlinear inelastic truss optimization based on improved k-nearest neighbor comparison and Rao algorithm. Structures 71, DOI: https://doi.org/10.1016/j.istruc.2024.108158.

[20] Grubits, P., Movahedi Rad, M. (2025). Automated elasto-plastic design of truss structures based on residual plastic deformations using a geometrical nonlinear optimization framework. Comput Struct 316, pp. 107855,

DOI: https://doi.org/10.1016/j.compstruc.2025.107855.
[21] W. Christensen, P., Klarbring, A. (2008). An Introduction to Structural Optimization.
[22] Michael Smith. (2009). ABAQUS/Standard User's Manual, Version 6.9.
[23] British Standards Institution. (2006). BS EN 10210-2:2006: Hot finnished structural hollow sections of non-alloy and fine grain steels - Part 2: Tolerances, dimensions and sections properties. British Standards Institution.
[24] Yun, X., Gardner, L. (2017). Stress-strain curves for hot-rolled steels. J Constr Steel Res 133, pp. 36–46, DOI: https://doi.org/10.1016/j.jcsr.2017.01.024.